Title
Towards the Efficient Design of Vehicular Ad-Hoc Networks

Author
Dulmage, Jared

Publication Date
2012

Peer reviewed|Thesis/dissertation

UNIVERSITY OF CALIFORNIA
Los Angeles

Towards the Efficient Design of Vehicular Ad-Hoc Networks

A dissertation submitted in partial satisfaction
of the requirements for the degree
Doctor of Philosophy in Electrical Engineering

by

Jared Dulmage

2012

ABSTRACT OF THE DISSERTATION

Towards the Efficient Design of Vehicular Ad-Hoc Networks

by

Jared Dulmage

Doctor of Philosophy in Electrical Engineering

University of California, Los Angeles, 2012

Professor Michael Paul Fitz, Chair

Large-scale wireless network design and analysis generally falls between two extreme approaches. The information theoretic approach trades scenario fidelity for analytical tractability. Its results often reveal fundamental design tradeoffs and performance limits under very generic assumptions. Numerical simulation campaigns capture the details of a particular network but at a high computational cost, precluding large-scale scenarios with many nodes. Because personal safety is at stake, the design of vehicular wireless networks poses a particularly daunting challenge, requiring both large-scale and highly detailed models. This dissertation aims to push information theoretic analysis towards reality and pull out detailed simulation in lieu of abstractions that improve its efficiency and, therefore, scalability.

The first analysis, however, facilitates the detailed simulation of a specific scenario on the highway. I present novel expressions for the time-domain correlations due to Doppler spectra proposed in the literature for modeling the highway propagation environment. The spectra are also re-interpreted to yield novel and intuitive non-isotropic angle-of-arrival scatterer profiles. Finally, I propose a sum-of-sinusoids software channel model that accurately synthesizes the fading paths' random processes.

In the second analysis, I take a semi-analytic approach to abstract the impact of the time-varying channel on effective throughput, or *goodput*, which accounts for physical layer overhead and re-transmission of lost packets. Based on an extensive simulation of a standard wireless vehicular network physical layer, I derive a set of expressions that can predict the goodput

given a number of signal, packet, and channel parameters. Further, I derive a metric that delimits the (nearly) optimal packet size (in the sense that it maximizes goodput) given the channel and signal parameters.

The third analysis extends the information theoretic statistics of an idealized orthogonal frequency division multiplexing (OFDM) system to one with practical constraints on channel estimation overhead. Incorporating heretofore separate results on channel estimation error, outage probability approximation, and goodput analysis, we identify a new tradeoff between the channel frequency-diversity and the training required to exploit that diversity. From this perspective, I find a novel optimization of the signal bandwidth of time-scalable OFDM transmissions to maximize goodput.

The final analysis derives new, closed form bounds and an approximation for the variance of narrowband vector transmissions in time-selective channels with training overhead. The bounds and approximation are shown to be accurate over a large range of channel and signal parameters. The expressions reveal the fundamental dependency of the variance on the product of the maximum Doppler shift and the vector duration.

The dissertation of Jared Dulmage is approved.

Mario Gerla

William Kaiser

Babak Daneshrad

Michael Paul Fitz, Committee Chair

University of California, Los Angeles

2012

To my wife Amy, the reason for all that I do.

TABLE OF CONTENTS

LIST OF FIGURES

LIST OF TABLES

ACKNOWLEDGMENTS

It takes a rare talent to meet a challenge as imposing as the completion of a doctoral program alone. After nearly a decade of sustained effort, I have more people to thank than most. I will start with my thesis advisor, Dr. Michael Fitz who, like an ancient mountaintop oracle, always had invaluable insights, advice and guidance, once you scaled the mountain to see him. Dr. Fitz exemplifies the kind of engineer to which I will continually strive. Next I would like to thank Deeona Columbia, UCLA Engineering Director of Student Affairs, who went above and beyond to give me a chance to succeed. She truly puts students interests first and is a genuine educator. Thanks also to Dr. Danijela Čabrić who gave me support when I was most at risk of losing it altogether.

I am the last member of my lab, the UCLA Wireless Research and Development (UnWiReD) lab. Through the years I had the pleasure of working alongside some incredibly talented and inspiring people. Thanks to Dr. David Browne and Dr. Heechoon Lee, models for industrious graduates anywhere. Thanks to Dr. Cong Shen and Dr. Michael Samuel for their continued friendship, language lessons, and general brilliance. Thanks to Dr. Daniel Liu, who demonstrated perseverance in the face of true adversity. Finally, thanks to Dr. Scott Enserink, a true friend, whose struggle somewhat mirrored my own. Scott was never too busy to offer help, support, or just an understanding ear.

Beyond my lab I had a number of special friends whose confidence in me never wavered. Thanks to Dr. Andres Vila Casado, eternal optimist and passionate lover of almost everything. Thanks to Dr. Esteban Valles who thought I could have finished 2 years ago. Thanks to my first roommates Bill Whitaker and Trevor Hayden who introduced me to Los Angeles. Finally, I want to thank the city of Los Angeles, a place whose creative energy permeates every corner coffee house, every alley, and every nondescript apartment complex. In the face of brutal criticism, the fortitude of Los Angelenos to make it their own way was simply inspiring.

Last but not least, I want to thank my wife Amy who put up with years of detached conversations and tech-speak. My thesis dedication says it all. I'd like to close by recalling some

advice from the first UnWiReD member I met when I started my studies. Ryan Penrod told me to take my time since "... the doctorate is a marathon, not a sprint." Yeah, no kidding.

VITA

1999	B.S. Electrical Engineering and Computer Science, Duke University, Durham, North Carolina.
1999–2003	Communications engineer, The MITRE Corporation, Eatontown, New Jersey.
2005–2010	Research Assistant, Electrical Engineering Department, University of California, Los Angeles, Los Angeles, California
2004	Engineering consultant, Metrozet LLC (formerly GeoSense), Los Angeles, CA
2007	Communications systems engineer, Northrop Grumman Aerospace Systems, Redondo Beach, California.
2008	M.S. Electrical Engineering, University of California, Los Angeles, Los Angeles, California
2010–present	Member of technical staff, Aerospace Corporation, El Segundo, California.
2012	Ph.D. Electrical Engineering, University of California, Los Angeles, Los Angeles, California

PUBLICATIONS AND PRESENTATIONS

J. Dulmage, T. Hoang, J. McConnell, M. Riehl, J. Wessel, and J. Peace, "Communications effects server-realistic communications effects for distributed simulations," In *MILCOM 2000. 21st Century Military Communications Conference Proceedings*, vol. 1, pp. 335–339, 2000.

J. Dulmage, C.A. Brooks and R. S. Wexler, “The Dynamic Frame Protocol,” In *MILCOM 2002, Proceedings* , vol. 1, pp. 7-11, 7–10 Oct. 2002.

J. Dulmage, M. Tsai, and M.P. Fitz, “COTS-based DSRC testbed for rapid algorithm development, implementation, and test,” In *WINTECH ’06, Proceedings*, pp. 113–114, 2006.

J. Dulmage and M.P. Fitz, “Non-Isotropic Fading Channel Model for the Highway Environment.” In *Vehicular Technology Magazine, IEEE*, vol. 2, no.4, pp.12–18, Dec. 2007.

J. Dulmage, M.P. Fitz, and D. Cabric, “A modulation dependent channel coherence metric for VANET simulation using IEEE 802.11p,” In *VTC Spring, IEEE Proceedings*, pp. 1–6, May 2010.

J. Dulmage and M.P. Fitz, “Reconfigurable Testbed for Rapid Algorithm Development, Implementation, and Test,” Presented at *WIVEC, 1st IEEE International Symposium on Wireless Vehicular Communications*, Oct. 2007.

CHAPTER 1

Introduction

1.1 The VANET Challenge

Intelligent Transportation Services (ITS) promise to improve transportation safety, efficiency, and comfort by coordinating vehicular flow, responding to events (such as accidents) quickly, providing on-the-move consumer services, and enhancing the authority's' ability to monitor, plan, and direct traffic. Its central enabling technology falls under the umbrella of vehicular ad-hoc networks (VANETs) which connect mobile vehicles and fixed roadside nodes through wireless links.

VANETs pose a significant challenge for system engineers. With safety-of-life at stake, the fidelity of predictive simulations and analytical design rules are particularly important. Typical urban or highway scenarios can involve hundreds or thousands of nodes communicating over novel, time-varying channels. Layers of the communication stack are intimately coupled with both the channela and mobility model as illustrated in Figure 1.1. This limits the applicability of analyses which isolate a single layer. For example, a warning message from one vehicle may cause nearby vehicles to alter their trajectory and relay further warnings, thus changing the network topology, message load, and characteristics of the propagation channel. To account for all of these effects, the entire aggregate model in Figure 1.1 needs to be simulated, which is computationally impractical. If the performance of one or more protocol layers could be expressed directly as a simpler function of the model parameters, then realism could be maintained while reducing computational cost.

Cross-layer analysis and design offers a compelling approach to designing, optimizing, and

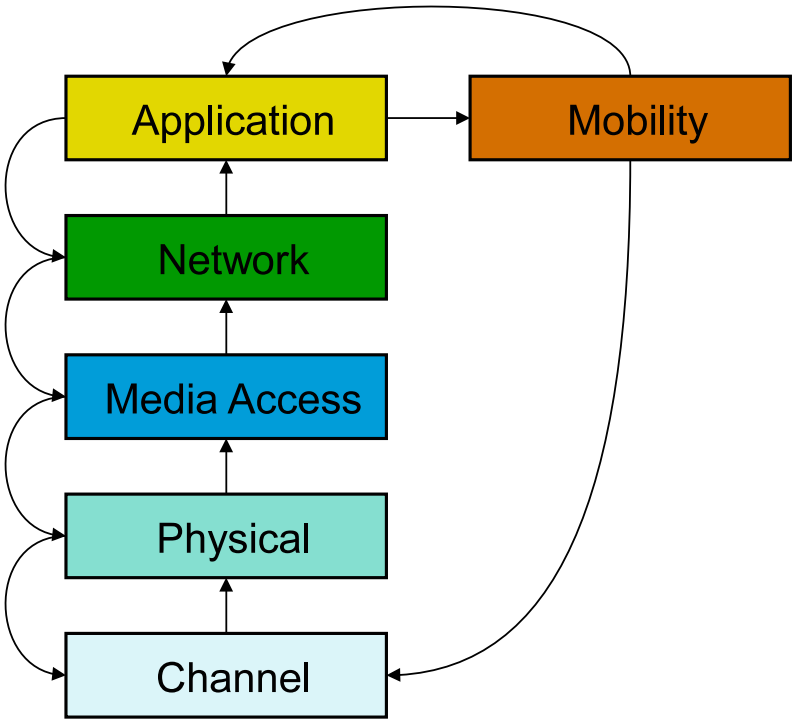

Figure 1.1: Block diagram illustrates the dependencies between typical protocol layers, the propagation channel, and the node mobility model. Arrows indicate an "influences" relationship. For instance, a GPS navigation application could direct where the node goes, influencing the mobility model.

implementing VANETs and ITS. By considering several layers of the communications stack at once, one can discern critical dependencies between parameters and formulate optimal solutions whose performance exceeds those determined using decoupled models. Such fidelity comes with a price: complexity. Cross-layer solutions are only as useful as the intuitive insights they offer through distillation of perhaps disparate parameters to a set of simplified critical aggregates. Often such solutions facilitate the adaptation of the parameters of one protocol layer to parameters or measurements taken from a different layer. Of particular importance is the cross-layer interaction between the physical layer (PHY) and the medium access control (MAC) layer. Each layer separately presents formidable challenges for accurate simulation, so accurate cross-layer models can simultaneously reduce development effort and increase practicable simulation fidelity and scale.

In this dissertation, I present a number of contributions that improve VANET model fidelity and identify relationships between PHY and MAC parameters that simplify system modeling while providing insights to assist in system design or guide adaptation while the system is operating.

1.2 Dissertation Summary

Wireless channel models link the theoretical and simulation realms to the real world by modeling the effect of the environment on wireless transmissions. To most precisely characterize system performance for a particular use scenario, a channel model specific to that scenario should be employed. Often, scenario-specific models are created from channel sounding campaigns that derive the salient statistical parameters from data captured through extensive experimentation.

Such a model was derived for vehicular networks operating on the highway, but only for implementation on a hardware channel emulator. In Chapter 2, I derive time-domain correlation functions for the set of unconventional Doppler spectra specified for the model, useful in system design and evaluation. I also re-interpret the spectra in the angular domain to reveal the

non-isotropic patterns of the incoming scattering components. The patterns validate the intuition that, on the highway, the strongest (e.g. closest) scatterers were concentrated to the sides of the vehicle, perpendicular to the axis of motion. I further propose an efficient sum-of-sinusoids software channel model that facilitates simulation of systems operating in the highway environment.

Dedicated Short Range Communications (DSRC) is an umbrella term referring to the wireless technologies over which ITS will operate. The IEEE 802.11p Wireless Access in Vehicular Environments (WAVE) [IEE06] standard is meant to be the most flexible and ubiquitous for both vehicle-to-vehicle (V2V) and vehicle-to-infrastructure (V2I) communications. IEEE 802.11p is a based on IEEE 802.11a and is similarly an orthogonal frequency division multiplexing (OFDM) waveform. Table 1.1 compares DSRC (IEEE 802.11p) with some other common wireless standards. As the leading candidate for the VANET wireless interface, analysis of IEEE 802.11p, a wideband OFDM waveform, operating over a realistic vehicular channel is the ultimate goal of my research. The contributions in this dissertation constitute a base upon which this goal could be reached.

In Chapter 3, I take a semi-analytic approach to cross-layer optimization of the PHY and MAC. I consider the *goodput*, or effective throughput accounting for PHY overhead and retransmission of lost packets by the MAC, of a DSRC transmission in the highway setting. Using the channel model derived in Chapter 2 and a IEEE 802.11p conformant PHY simulation model, I derive a novel expression for the cross-layer spectral efficiency (i.e. the goodput per unit bandwidth) through a curve fit to an empirical curve generated through an extensive simulation campaign. I identify a tradeoff between goodput and the packet length and propose a modified coherence time metric that accounts for the PHY transmission mode. This metric predicts the packet length that maximizes the system goodput more accurately than the traditional coherence time. The result has implications for channelization of the DSRC allocated spectrum assuming use of proportionally time-scaled DSRC waveforms, a matter actually considered in the IEEE 802.11p standardization process.

The semi-analytic approach yields accurate solutions to specific scenarios, but provides less

Table 1.1: Comparison of wireless communications systems.

	DSRC	802.11 Wi-Fi	Cellular	Mobile WiMAX
Data Rate	3-27 Mbps	6-54 Mbps	$<$2 Mbps	1-32 Mbps
Latency	$<$50 ms	seconds	seconds	n/a
Range	$<$1 km	$<$100 m	$<$10 km	$<$15 km
Mobility	$>$60 mph	$>$5 mph	$>$60 mph	$>$60 mph
Nominal Bandwidth	10 MHz	20 MHz	$<$3 MHz	$<$ 10 MHz
Operating Band	5.86-5.92 GHz (ITS-RS)	2.4/5.2 GHz (ISM)	800 MHz, 1.9 GHz	2.5 GHz
IEEE std.	802.11p (WAVE)	802.11g/a	n/a	802.16e

insight and general applicability than could a purely analytic approach. Information theoretic analysis provides invaluable guidance for system design, reveals fundamental parameter tradeoffs and performance limits, though lacks the scenario specific details of simulation. The second half of this dissertation I extend information theoretic analyses in the literature to incorporate more realistic signal models.

In Chapter 4, I combine heretofore separate analyses: the optimization of the training overhead in pilot-symbol assisted modulation (PSAM-)OFDM to maximize average achievable rate and the use of mean and variance statistics of (non-PSAM) OFDM (with perfect channel state information) to approximate its outage probability. I present two expressions that extend those for the mean and variance of the mutual information (MI) of OFDM in quasi-static, multipath Rayleigh fading to account for sub-carriers used for channel estimation (i.e. pilots). The main contribution of this work is the identification of a tradeoff between the frequency-diversity offered by the channel (reflected by the MI variance) and the training overhead required to exploit that diversity. This has implications for channelization similar to that in Chapter 3 but considering general data rates and symbol-by-symbol channel estimation. The analysis enables maximization of the achieved goodput, which is greater than that achieved optimizing either the (ergodic) average MI or variance (as proposed in the literature).

While the analysis in Chapter 4 provides a means for optimization of goodput, it relies on numerical evaluation of the MI variance. This provides limited insight into the dependence of the variance, and hence the goodput optimal PHY rate, on other system parameters. In Chapter 5 I derive closed form bounds and an accurate approximation for the MI variance of narrowband transmissions in time-varying fading. A narrowband system was considered to build upon the existing literature, however the results have a dual solution in the frequency-domain for wideband PSAM-OFDM systems operating over independent, identically distributed multipath Rayleigh channels. The main contribution of this chapter shows that, operating over a time-varying channel with a rectangular Doppler spectrum, the MI variance is bound (both upper and lower) by the inverse of the product of the maximum Doppler shift and the transmission block size (at a fixed SNR). From these bounds I derive a novel approximation for the MI vari-

ance that is shown to be quite accurate across a range of channel and block parameters. The analysis presented in this chapter could potentially be extended to compute the MI variance of OFDM tranmissions in doubly-selective (though varying slowly enough in time to ignore inter-carrier interference) channels which would be of great use in accurately predicting good-put performance of modern OFDM-based systems as well as provide expressions from which to optimize and adapt parameters.

CHAPTER 2

Non-Isotropic Fading Channel Model for the Highway Environment

2.1 Introduction

Intelligent Transportation Systems (ITS) promises to revolutionize travel by enabling mobile units to communicate among themselves and with non-mobile stations over wireless communications links. The ITS infrastructure will make advanced traffic management, remote safety alerts, and interactive consumer services possible on-the-move at speeds up to and exceeding those on the highway.

2.2 Background and Motivation

The high-speed, mobile-to-mobile scenario presents a unique wireless environment. The Wireless Access in Vehicular Environments (WAVE) draft standard document [IEE06] describes the channel model recommended for system development and test. The model was derived from channel sounding experiments performed in an open highway environment [AIT04]. The standard specifies a 10-tap multipath fading model with the majority of taps exhibiting Rician fading. The diffuse Doppler spectrum for each tap results from the non-isotropic nature of the environment and does not match the classic Jakes spectrum. This chapter explores the alternative Doppler spectra and their realization using a sum-of-sinusoids (SoS) channel model suitable for algorithm development and test.

The following describes the outline of this chapter: section III introduces the ideal channel

model, section IV describes the simulation model used for test, section V briefly compares the simulated model statistics to the proposed reference model, and section VI states conclusions and future efforts.

2.3 Model Description

The multipath channel model described in [IEE06] consists of ten independent, Rician faded taps. Each tap is parameterized by an overall gain, excess tap delay, Rice K-factor, specular angle-of-arrival, frequency offset, Doppler spectrum half-width, and Doppler spectrum shape. The following idealized model applies to each tap, ignores the frequency offset, and treats the Doppler spectrum half-width as the maximum Doppler shift.

2.3.1 Rician Fading Process

The reference model is the 2-D Rician, non-isotropic scattering model. The following equation describes the complex baseband Rician fading process:

$$z(t) = x(t) + y(t) \tag{2.1}$$

where $x(t)$ is the diffuse component given by

$$x(t) = x_I(t) + jx_Q(t) \tag{2.2}$$

and $x_I(t)$ and $x_Q(t)$ are independent identically distributed (IID) Gaussian random processes with mean μ=0 and variance $\sigma^2/2$. The function y(t) is the specular or line-of-sight (LoS) component and is specified as

$$y(t) = \rho e^{j\omega_0 t + j\theta_0} \tag{2.3}$$

where $\omega_0 = 2\pi f_m \cos(\alpha_0)$ is the LoS angular Doppler with LoS angle-of-arrival (AoA) α_0 and maximum Doppler f_m in hertz, and θ_0 is the LoS phase. The average fading signal power is given by

$$G = E[\|z(t)\|^2] = E[< z(t)z^*(t) >] \tag{2.4}$$

where $< \ldots >$ is the time average. Let $K \geq 0$ be the ratio of the specular power to the diffuse power. We can write the LoS amplitude ρ and the total diffuse power σ^2 as

$$\rho = \sqrt{GK/(1+K)} \tag{2.5}$$

$$\sigma^2 = G/(1+K). \tag{2.6}$$

The Rician process naturally degenerates to a Rayleigh process by setting K=0. Using (2.5) and (2.6) the probability density function (pdf) of the fading signal envelope $r(t) = |z(t)|$ is [Stu01]

$$p_r(r) = \frac{2r(1+K)}{G} e^{-K-(1+K)r^2/G} I_0\left(2r\sqrt{K(1+K)/G}\right) \tag{2.7}$$

where $I_0(\cdot)$ is the zero order modified bessel function of the first kind. The cumulative distribution function (cdf) is [Stu01]

$$P_r(r \leq R) = \int_{-\infty}^{R} p_r(r)dr = 1 - \mathrm{Q}(\sqrt{2K}, \sqrt{2(1+K)\nu^2}) \tag{2.8}$$

where Q(a,b) is the marcum-Q function and $\nu = R/\sqrt{G}$ is the root-mean-square (rms) normalized envelope level. The pdf of the phase $\theta(t) = \angle z(t)$ of the fading signal is [PKL98]

$$p_\theta(\theta,t) = \frac{1}{2\pi} e^{-K}\left(1 + \sqrt{\pi K}\Phi_\theta(t) e^{K\Phi_\theta^2(t)} \times \left(1 + \mathrm{erf}\left(\sqrt{K}\Phi_\theta(t)\right)\right)\right) \tag{2.9}$$

where $\Phi_\theta(t) = \cos(\theta - \theta_0 - \omega_0 t)$ and $\theta \in [-\pi, \pi)$. Note that the phase becomes time invariant for $\omega_0 = 0$ (via $\alpha_0 = \pi/2$) and tends to the uniform distribution $p_\theta(\theta) = 1/2\pi$ as $K \to 0$.

2.3.2 Fading Process Correlations

The fading process $z(t)$ can be separated into a diffuse component and specular component. Similarly we can separate those components of the fading signal correlations. This decomposition facilitates the analysis of alternative diffuse processes independent of the overall fading signal. In this vein, the correlations of the Rician fading process $R_{g(z)}(\tau)$ are expressed in terms

of the autocorrelation function of the diffuse component $R_{xx}(\tau)$

$$R_{zz}(\tau) = \frac{G}{1+K}\left(R_{xx}(\tau) + Ke^{j\omega_0\tau}\right) \tag{2.10a}$$

$$\begin{aligned} R_{z_I z_I}(\tau) &= \frac{1}{2}\Re R_{zz}(\tau) \\ &= \frac{G}{2+2K}\left(\Re R_{xx}(\tau) + K\cos(\omega_0\tau)\right) \end{aligned} \tag{2.10b}$$

$$\begin{aligned} R_{z_I z_Q}(\tau) &= \frac{1}{2}\Im R_{zz}(\tau) \\ &= \frac{G}{2+2K}\left(\Im R_{xx}(\tau) + K\sin(\omega_0\tau)\right) \end{aligned} \tag{2.10c}$$

$$\begin{aligned} R_{|z|^2|z|^2}(\tau) &= \left(\frac{G}{1+K}\right)^2 \left(1+2K+K^2\right. \\ &\quad \left. + R_{xx}^2(\tau) + 2KR_{xx}(\tau)\cos(\omega_0\tau)\right) \\ &= \left(\frac{G}{1+K}\right)^2 (1+2K) + |R_{zz}(\tau)|^2 \end{aligned} \tag{2.10d}$$

2.3.3 Diffuse Doppler Spectra

Motion in the wireless environment causes transmitted signals to experience Doppler shifts as a function of the angle between the signal path and the direction of motion. Signals arrive at a receiver after having experienced reflections from potentially moving scatterers at a variety of angles. The superposition of these multipath components with a range of Doppler shifts and received powers manifests as a Doppler spectrum at the receiver. The exact shape of the Doppler spectrum is a function of the wireless environment. Annex Q of [IEE06] describes several Doppler spectra considered for matching against data taken from channel sounding experiments. Figure 2.1 illustrates each candidate spectrum.

The (unnormalized) Doppler power spectral density (DPSD) functions for the JakesX, round,

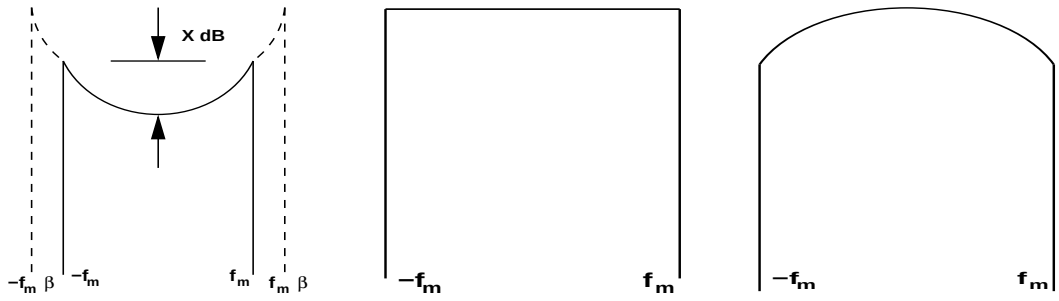

(a) (b) (c)

Figure 2.1: Diffuse spectra: a) JakesX (windowed Jakes), b) Flat, c) Round.

and flat spectrum shapes respectively are

$$S_X(f) = \begin{cases} \beta\left(\pi f_m \sqrt{1-(\beta f/f_m)^2}\right)^{-1}, & |f| \le f_m, \\ 0, & \text{otherwise}, \end{cases} \tag{2.11a}$$

$$S_r(f) = \begin{cases} \pi f_m \sqrt{1-(f/f_m)^2}, & |f| \le f_m, \\ 0, & \text{otherwise}, \end{cases} \tag{2.11b}$$

$$S_f(f) = \begin{cases} 1, & |f| \le f_m, \\ 0, & \text{otherwise}, \end{cases} \tag{2.11c}$$

where f_m is the maximum Doppler shift and $\beta = \sqrt{1-10^{-X/5}}$ where $X \ge 0$ is in dB (thus $0 \le \beta \le 1$). The JakesX spectrum becomes the classic Jakes spectrum as $X \to \infty$ or equivalently $\beta \to 1$.

2.3.4 Diffuse Process Correlations

The inverse Fourier transforms of the Doppler spectra of (2.11) result in the corresponding time-domain signal autocorrelation functions

$$R_X(\tau) = \frac{2}{\pi}\int_0^{\gamma} \cos(2\pi f_m \tau \sin\alpha)\, d\alpha \tag{2.12a}$$

$$R_r(\tau) = \pi^2 f_m^2 \frac{J_1(2\pi f_m \tau)}{2\pi f_m \tau} \tag{2.12b}$$

$$R_f(\tau) = 2 f_m \,\mathrm{sinc}(2\pi f_m \tau) \tag{2.12c}$$

where $\mathrm{sinc}(x) = \sin(x)/x$, $J_1(x)$ is the first order Bessel function, and $\gamma = \arcsin(\beta)$ with $0 \leq \gamma \leq \pi/2$.

2.3.5 Angle of Arrival (AoA) Distributions

Jakes expressed the bandpass DPSD in terms of the pdf of the angle of arrival $p(\alpha)$ and the antenna gain pattern $G(\alpha)$ in the horizontal plane. The diffuse complex baseband DPSD is given by

$$S_{xx}(f) = S_{II}(f) + S_{QQ}(f) = 2S_{II}(f). \tag{2.13}$$

where $S_{II}(t) = S_{QQ}(t)$ are the in-phase and quadrature spectra of the IID random processes $x_I(t)$ and $x_Q(t)$ respectively. Substitute (2.13) into the relationship between the baseband and bandpass spectra $S_{ss}(f)$ to get

$$S_{ss}(f) = \frac{1}{2}(S_{xx}(f-f_c) + S_{xx}(-f-f_c)) = S_{II}(f-f_c) + S_{II}(-f-f_c) \tag{2.14}$$

where f_c is the carrier frequency. Comparing (2.14) with (2.13) we observe that the baseband spectrum is a scaled, frequency shifted duplicate of the one-sided bandpass spectrum. We can thus apply Jakes analysis [JC94] to the complex baseband case through $S_{II}(f)$.

$$S_{II}(f) = \frac{b}{f_m\sqrt{1-(f/f_m)^2}}\left[p(\alpha)G(\alpha) + p(-\alpha)G(-\alpha)\right] \tag{2.15}$$

where b is the effective isotropic received power (EIRP). The value of b is nominally the transmit power multiplied by the maximum antenna gain. Because our Doppler spectra are known,

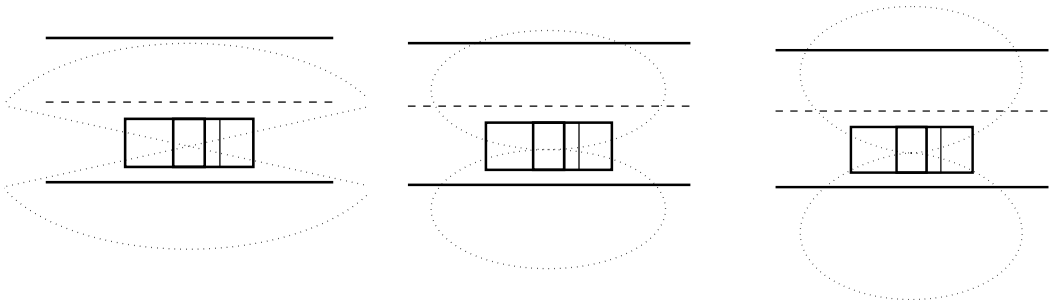

(a) (b) (c)

Figure 2.2: Angle-of-Arrival distributions for a) JakesX, b) flat, and c) round spectra. Vehicle and roadway included for scale reference.

we restate ((2.15)) to isolate $p(\alpha)$ and $G(\alpha)$.

$$p(\alpha)G(\alpha)+p(-\alpha)G(-\alpha)=\frac{S_{II}(f)f_m\sqrt{1-(f/f_m)^2}}{b}. \tag{2.16}$$

Without loss of generality assume a unit gain, isotropic antenna $G(\alpha)=1$ and unit transmit power such that $b=1$. Since all of the desired spectra (2.11) are symmetric, the right hand side of (2.16) is symmetric and we can assume a symmetric AoA distribution $p(\alpha)=p(-\alpha)$. Normalizing each desired spectrum $S_{(\cdot)}(f)$ in (2.11) by $R_{(\cdot)}(0)$ in (2.12) and using the fact that $\sqrt{1-(f/f_m)^2}=|\sin(\alpha)|$ [JC94] we get the following AoA pdfs:

$$p_X(\alpha)=1/4\gamma, \qquad |\alpha-\frac{\pi}{2}|\leq\gamma \tag{2.17a}$$

$$p_r(\alpha)=\sin^2(\alpha)/\pi, \qquad |\alpha|\leq\pi \tag{2.17b}$$

$$p_f(\alpha)=|\sin(\alpha)|/4, \qquad |\alpha|\leq\pi \tag{2.17c}$$

where the range of α in (2.17a) results from the requirement that $\int p_{cX}(\alpha)d\alpha=1$ and that the range of f in (2.11a) is centered about $f=0$ or $\alpha=\arccos(f/f_d)=\pi/2$. Recall sub-scripts X, r, and f refer to the JakesX, round, and flat Doppler spectra, respectively (2.11). Figure 2.2 is a geometric interpretation of each distribution in (2.17) that illustrates the non-isotropic incidence of scatterer power.

2.3.6 Level-Crossing Rate and Average Fade Duration

The level-crossing rate (LCR) L_R and average fade duration (AFD) $\bar{T}$ are two statistics commonly employed to validate the accuracy of channel models [JC94,Stu01,PKL98]. These statistics are functions of the moments of the Doppler spectrum. These functions have a closed form for Rician fading as long as the diffuse spectrum is symmetric and the specular AoA is $\pi/2$ (i.e. $\omega_0 = 0$) [Stu01]. Patzold [PL99] gives the equations as

$$L_R = \sqrt{\frac{b_2}{2\pi}} p_r(R) \tag{2.18}$$

$$\bar{T} = P_r(r \leq R)/L_R \tag{2.19}$$

where b_2 is the second moment of the in-phase component of the diffuse DPSD, R is the envelope level and $p_r(R)$ and $P_r(r \leq R)$ are given in (2.7) and (2.8) respectively. The value b_2 can be computed using [JC94]

$$b_2 = (2\pi)^2 \int_{-\infty}^{\infty} S_{II}(f) f^2 df \tag{2.20}$$

Applying this to each spectrum in (2.11) results in

$$b_{2_X} = \frac{\pi^2 f_m^2}{\beta^2} \left(1 - \frac{\beta\sqrt{1-\beta^2}}{\gamma} \right) \tag{2.21a}$$

$$b_{2_r} = \frac{\pi^2 f_m^2}{2} \tag{2.21b}$$

$$b_{2_f} = \frac{2\pi^2 f_m^2}{3}. \tag{2.21c}$$

Substitute (2.21) normalized by the diffuse power of $x_I(t)$ ($\sigma^2/2$) (2.6) and (2.7) into (2.18) to get

$$L_{R_X} = \sqrt{\frac{1-\beta\sqrt{1-\beta^2}}{\beta^2\gamma}} \Lambda(\nu) \tag{2.22a}$$

$$L_{R_r} = \sqrt{\frac{1}{2}} \Lambda(\nu) \tag{2.22b}$$

$$L_{R_f} = \sqrt{\frac{2}{3}} \Lambda(\nu) \tag{2.22c}$$

where $\nu = R/\sqrt{G}$ is the rms normalized signal level as in (2.8), $\gamma = \arcsin(\beta)$ as in (2.12), and

$$\Lambda(\nu) = \sqrt{2\pi(1+K)} f_m \nu e^{-K-(1+K)\nu^2} \times I_0\left(2\nu\sqrt{K(1+K)}\right) \tag{2.23}$$

is the LCR of the 2-D isotropic scattering environment with a Jakes spectrum [Stu01]. The AFD follows directly from (2.8) and (2.22).

2.4 Simulation

2.4.1 Channel Model

Clarke's sum-of-sinusoids [Cla68] model was chosen as the basic channel model for simulations. The model was modified to select Doppler frequencies according to the various AoA distributions of (2.17). An exponential term was added to produce a Rician fading process. The final modified channel model is

$$Z(t) = \sqrt{\frac{G}{1+K}}\left(X(t) + \sqrt{K}e^{j\omega_0 t + j\theta_0}\right) \tag{2.24a}$$

$$X(t) = \sqrt{\frac{1}{N}}\sum_{n=1}^{N} e^{j\omega_n t + j\theta_n} \tag{2.24b}$$

where $\omega_n = f_m \cos(\alpha_n)$ is the diffuse Doppler with random AoA $\alpha_n \sim p_s(\alpha)$ for path n, $p_s(\alpha)$ is given in (2.17), and $\theta_n \sim U(-\pi, \pi)$ is the random diffuse phase. All other parameters follow the convention set forth in section 2.3.1. We omit further details of this model and its analytical correlations and refer interested readers to the references [Cla68].

2.4.2 Random Doppler Generation

The probability density functions for the angles-of-arrival of the flat and round Doppler spectra are non-standard distributions. As such no generation functions specific to these distributions are available. A simple and generic procedure for generating random numbers from an arbitrary distribution is Von Neumann's rejection method [Grz89]. Briefly, generate two uniform random numbers $a \in D$ and $b \in R$ where D and R are the domain and range of the desired pdf $p(x)$ respectively. Accept a as a valid random number from $p(x)$ if $b < p(a)$. Repeat until an acceptable number is generated.

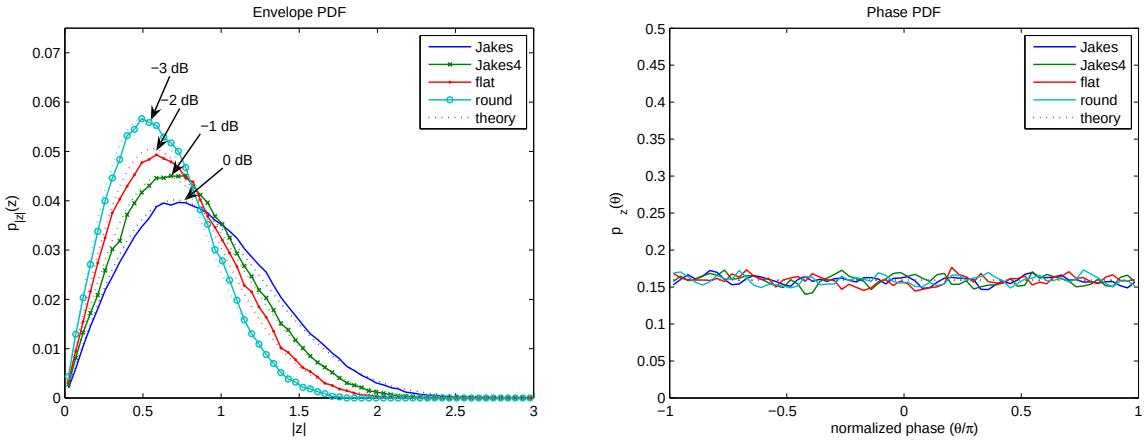

(a) (b)

Figure 2.3: Fading signal a) envelope pdf, b) phase pdf. Gain G=0,-1,-2,-3 dB to separate plots.

Intuitively the method is akin to randomly throwing darts at a graph of the target distribution and accepting the x coordinate as the realization when the dart hits below the distribution function. The domains of the target distributions in (2.17) are restricted to finite ranges ($|\alpha| \leq \pi$) which makes this technique especially attractive (imagine the difficulty of throwing darts at an infinitely long dart board).

2.5 Results

Simulated channels were generated from the above model using each of the new target Doppler spectra AoA distributions. Unless otherwise stated, statistics and correlations are averaged over 400 channels, $f_m = 1$ kHz, $K = 0$.

2.5.1 Envelope and Phase Probability Distributions

Figure 2.3a and Figure 2.3b show the envelope and phase distributions. They match well with the theoretical ideal plots.

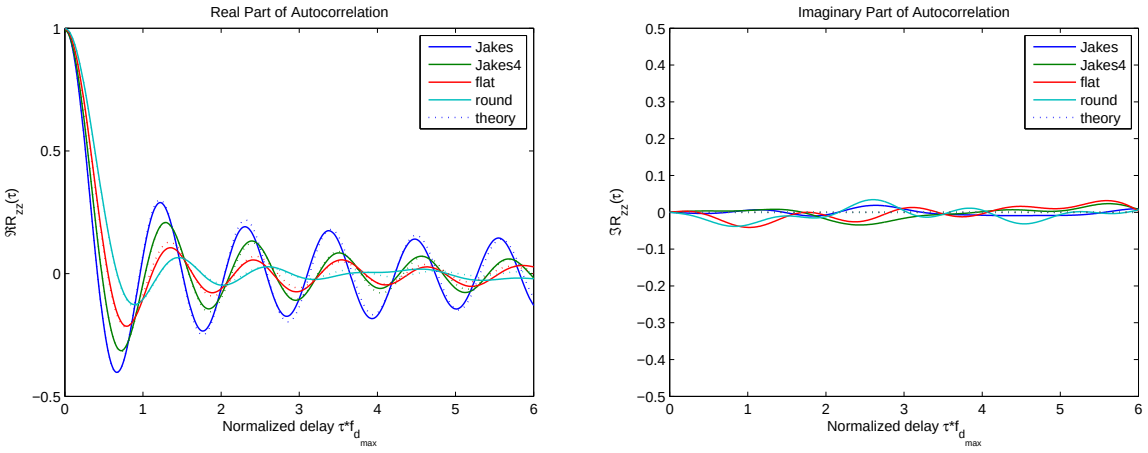

(a) (b)

Figure 2.4: Fading signal autocorrelation a) real part, b) imaginary part.

2.5.2 Channel Correlations

Figure 2.4a and Figure 2.4b show the real and imaginary parts of the autocorrelation of the fading signal. The autocorrelations have progressively wider main lobes with steeper envelope rolloffs as the proportion of power contained at the higher Doppler shifts is reduced.

Figure 2.5 shows the squared envelope autocorrelations. The plots show good approximation of the reference shape. The error is due mostly to the underlying model error [Cla68,Pat06].

2.5.3 Level Crossing Rates and Average Fade Duration

Figure 2.6a and Figure 2.6b show the simulated Doppler normalized level-crossing rate (L_R/f_m) and average fade duration ($\bar{T} * f_m$).

2.6 Conclusion

This chapter derived the angles-of-arrival distributions for several non-Jakes spectra considered in highway scenario channel models. The theoretical correlations, level-crossing-rates, and

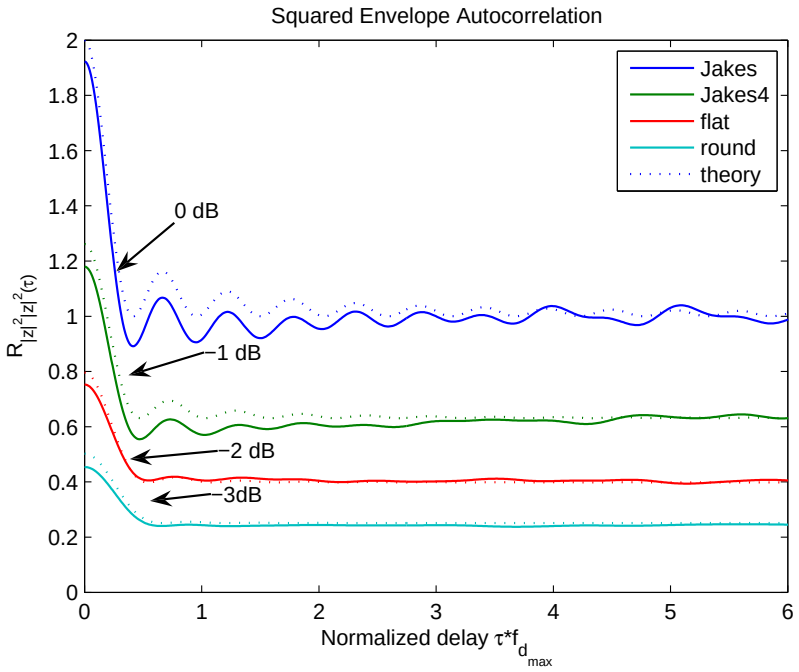

Figure 2.5: Squared envelope autocorrelation. Gain G=0,-1,-2,-3 dB to separate plots.

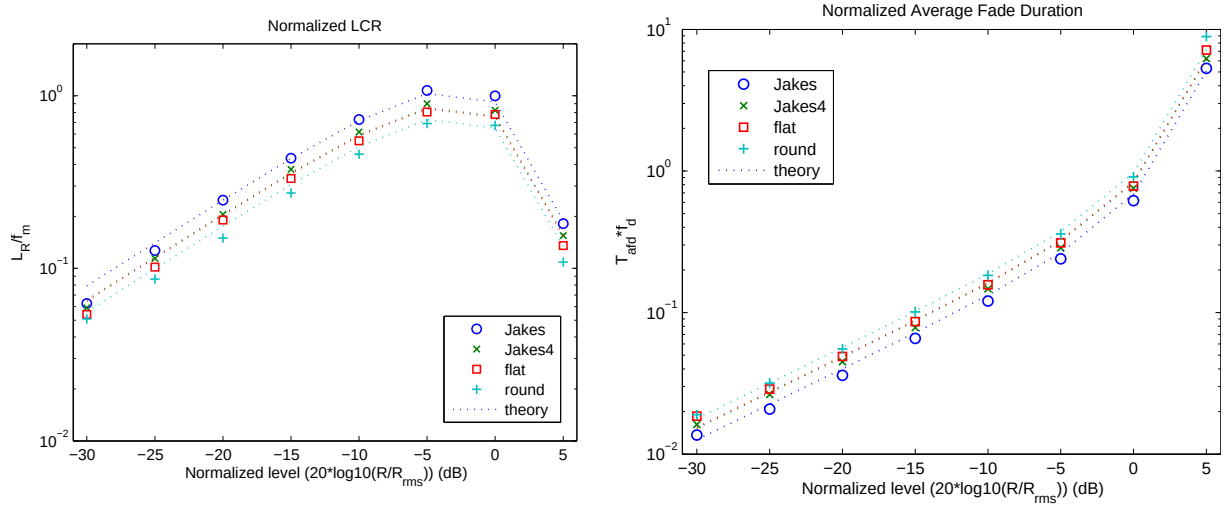

(a) (b)

Figure 2.6: Normalized a) level-crossing rate, b) average fade duration.

average-fade-durations were derived. The Clarke channel model was modified to generate the new fading signals. Analysis of the simulation results demonstrates the agreement of the model with theory. More efficient generation of these non-isotropic spectra may be realized using deterministic models akin to the Method of Exact Doppler Spread (MEDS) [PKL98]. Further generalization could incorporate the frequency offsets stipulated in the 802.11p/D1.0 channel model would add additional realism to the model.

CHAPTER 3

A Modulation Dependent Channel Coherence Metric for VANET Simulation using IEEE 802.11p

3.1 Introduction

Vehicular networks exist in inherently time-varying environments. For accurate simulation the variation of the channel with time must be taken into account. Traditionally, coherence time has been used for this purpose. Typical IEEE 802.11p receivers do not track the channel in time [YEY04]. Common to most IEEE 802.11 receivers, channel estimates using the preamble at the beginning of the packet are maintained constant throughout the duration of the packet. The pilots embedded in each OFDM symbol are used only for frequency offset tracking. The assumption is that as long as the packet duration is less than the coherence time of the channel, the channel will have not changed significantly from the initial preamble and the average error rate performance will be dictated by the instantaneous signal-to-noise ratio (SNR). This basic performance can be found analytically or through simulations over a typical, time-invariant channel. Common physical layer (PHY) models used in network simulation compute packet errors based on the resulting average bit error rate (BER) curves or an SNR threshold set according to the target error rate (essentially a binary partitioning of the BER curve). More complex channel estimation algorithms that track the channel throughout the packet have been proposed but are not in the scope of this chapter, which focuses on the more common case described.

While it is convenient to assume that a packet shorter than the coherence time of a channel experiences no degradation due to the channel time-variation, this chapter shows this to be false. It is also false to assume that a packet longer than the coherence time will be severely degraded.

The severity of degradation depends on the signal and receiver structures as well. In time-varying channels, the channel estimates derived from the initial preamble lose coherence with the channel over the duration of the packet. Thus, longer packets experience greater error rates due to accumulated channel estimation error [SCE02]. This applies even to the slow-fading scenario, which is the focus of this chapter, where the channel is essentially invariant over the symbol duration and there is negligible ICI.

Several papers have addressed error rate performance of uncoded narrowband communications over quasi-static channels accounting for imperfect channel state information (CSI) for both single-input single-output [SA95, TAG99] and multiple-input multiple-output [CB04, TC06] systems. Analysis in [FGS99] applied to coded modulation in correlated fading but with perfect CSI. A narrowband bit-interleaved, coded modulation system with imperfect CSI was analyzed in [HR03] for 16QAM symbols only. In all of these analyses the error rate was not related to either the packet length or coherence time of the channel. In most cases, the channel was considered quasi-static, varying independently from symbol to symbol. None of the analyses applied directly to a practical system or standard. The authors of [SCE02, SCE03] investigated the transmission efficiency of IEEE 802.11R/A, a short-lived precursor to the current IEEE 802.11p standard, over time-varying channels. Using simulated packet error rate (PER) versus velocity curves, they computed the ratio of the ideal transmission time of a packet to that including physical and link layer overhead.

This chapter defines and quantifies a new metric, the normalized empirical coherence time (NETC). The NETC provides a more accurate estimate of the time over which a system may be considered unaffected by the time-varying channel. The metric demarcates the greatest time, normalized by packet duration, such that the system performance is degraded by some percentage. It is an explicit function of modulation. By dint of its derivation from empirical PER curves, similar to [SCE02], the metric implicitly accounts for the signal, receiver, and channel structures which determine the underlying PER. These results have particular relevance to the simulation of VANETs which tend to operate over time varying channels and whose appropriate packet lengths are unknown.

Table 3.1: Parameter settings for simulation campaign.

Parameter	Set
SNR	30 dB
Packet length	2 – 30 OFDM symbols
Modulation	BPSK, QPSK, 16QAM, 64QAM
Bandwidth	2.5, 5, 10, 20 MHz

3.2 System Model

A baseband equivalent IEEE 802.11 OFDM model was used for an extensive simulation campaign. We assume that the received signal distortion is solely from the doubly-selective channel. Thus we assume ideal time and frequency synchronization. The receiver generated channel estimates from the long training sequence (LTS) of the packet preamble using a zero-forcing estimator. The frequency domain observations, along with the channel estimates, were input to a mismatched detector which generated approximate log-likelihood ratios subsequently input to a hard-decision Viterbi decoder. Embedded pilots were not used for channel tracking. While the model was sub-optimal compared to maximum-likelihood detection, it was representative of typical practical implementations.

3.2.1 System Parameters

A number of system parameters were swept across a range of values summarized in Table 3.1. By setting high SNR, any observed performance degradation would be dominated by channel estimation error and not noise. Packet lengths are set in terms of OFDM symbols to fix the packet duration across modulations. The packet length in bytes is proportional to the modulation order (equivalently the PHY rate). As a convention for each modulation, the minimum coding rate available by the standard was set, that is $1/2$ for BPSK, QPSK, and 16QAM and $2/3$ for

64QAM. In this chapter "packet" refers to the PLCP protocol data unit (PPDU) in the standard [IEE03].

While 10 MHz is the nominal bandwidth of IEEE 802.11p transmissions, there has been discussion of optional support for 5 and 20 MHz channels [SCH07, IEE06]. Packet duration is inversely proportional to the signal bandwidth, thus a 5 MHz signal would be twice as long as the 10 MHz signal. The 2.5 MHz channel was included as an extreme case (i.e. the longest packet duration). By using a number of bandwidths, we can isolate the affect of modulation on the error rate. For example, a 5 symbol, 10 MHz signal with BPSK modulation has the same number of bits as a 5 symbol, 5 MHz signal with QPSK modulation. Thus both the packet duration and the codeword length are equal. Any discrepancy in performance will be due to the modulation.

3.2.2 Channel Parameters

The channel model was a wide-sense stationary, uncorrelated scattering model. Several channels were used in the simulations: a set of canonical channel models (CC) and an Expressway channel model (GEC) derived from a channel sounding campaign by researchers at the Georgia Institute of Technology ([IEE06, Annex Q], [Pat06]). The CC have conventional, though synthetic scattering functions whereas the GEC models a realistic channel. The CC scattering function is exponential in delay and uniform in Doppler. That is, the gain g_l and Doppler spread f_{D_l} of tap $l = 1..L$ with delay τ_l are

$$g_l = Ce^{-a\tau_l} \quad \text{and} \quad f_{D_l} = f_D, \tag{3.1}$$

respectively. The decay rate a of the tap gains is set to engender a particular coherence bandwidth [Rap96]

$$B_C \triangleq 0.2/\tau_{rms} \tag{3.2}$$

where $\tau_{rms} = \sqrt{\sum_{l=1}^{L} g_l \tau_l^2}$ and $\tau_l < T_{CP}$ the cyclic prefix duration. Equivalently $L < BT_{CP}$ where B=10 MHz is the channel bandwidth. The normalizing constant C ensured that the channel had unit gain (i.e. $C^{-1} = \sum_{l=1}^{L} e^{-a\tau_l}$). The gains were constrained such that $10\log_{10}(g_1/g_L) \leq 30$ dB.

Table 3.2: Channel parameters for simulation campaign.

Parameter	CC	GEC
L	3–15	11
τ_L	300–1500 ns	450 ns
τ_{rms}	26.6–200 ns	48 ns
B_C	1–7.5 MHz	4.2 MHz
f_D	1.3–26.4 kHz	0.813 kHz
T_C	16–320 μs	520 μs
k_1	0 dB	21.9 dB
g_1/g_L	30 dB	28 dB
$S(f)$	Jakes	varied*

* see [IEE06, Annex Q]

Recall for the CC $g_1 > g_2 > \ldots > g_L$.

The uniform Doppler spread f_D was set to engender a particular coherence time T_C as defined by [Rap96]

$$T_C \triangleq 0.423/f_D \tag{3.3}$$

where $f_D = 2\pi\sqrt{\int f^2 S(f)df}$ and $S(f)$ is the (normalized) power spectral density of the Doppler spectrum. For the classic Jakes spectrum used for the CC, $f_D = \sqrt{2}\pi f_m$ where f_m is the maximum Doppler shift. The Doppler spectra for the GEC are not the Jakes spectrum, however their Doppler spreads are upper bounded by those of the Jakes spectrum. Table 3.2 summarizes the channel parameters for both the CC and GEC.

Because the CC were intended to act as a proxy for V2V channels, a line-of-sight component was assumed. The first tap Rice K-factor is given as k_1. The CC were not meant to emulate a real

channel but to serve as references for channels with particular coherence time and coherence bandwidth measures. The coherence times are chosen to be comparable to the packet durations such that the coherence time to packet duration ratio is in the neighborhood of one.[1]

3.3 Methodology

For the vehicular scenario motivating our research, safety applications are a particular priority. These applications have strict latency and reliability requirements. Our performance metric is point-to-point link layer throughput. This metric is inversely proportional to latency. Thus a maximum latency constraint would correspond to a minimum throughput, given some message size (in bytes). Throughput also gives an upper bound on the number of users supported by a particular link. For example, if the supported link throughput is 1 Mbps and the tolerable latency is 20 ms for a 500 bit message, then $10^6/500 \times 0.02 = 40$ users could be supported with perfect scheduling.

At a high level, PER curves are obtained via simulation of a typical IEEE 802.11p system for a range of modulations, packet lengths, signal bandwidths, and channel coherence times. The PER curves are transformed to throughput via calculations detailed in the sequel. Trends in the throughput versus coherence time, packet duration ratio are fit to an analytical expression. The expression is then used to define the NETC.

3.3.1 Packet Error Rate

Simulations were run for a minimum of 10000 packets or 400 packet errors. We were interested in degradation due solely to accumulated channel estimation error. Because the channel estimation algorithm uses the preamble LTS, as long as $f_D \ll f_\Delta$, where $f_\Delta = B/64 \approx 156$ kHz is the sub-carrier separation, the frequency-domain estimates were not significantly degraded by ICI. In order to ensure that the channel impulse response remained within the duration of the

[1] For curious readers, the CC coherence times correspond to mobile speeds of approximately 34 to 675 mph (55 to 1086 km/h) at an operating frequency of 5.9 GHz.

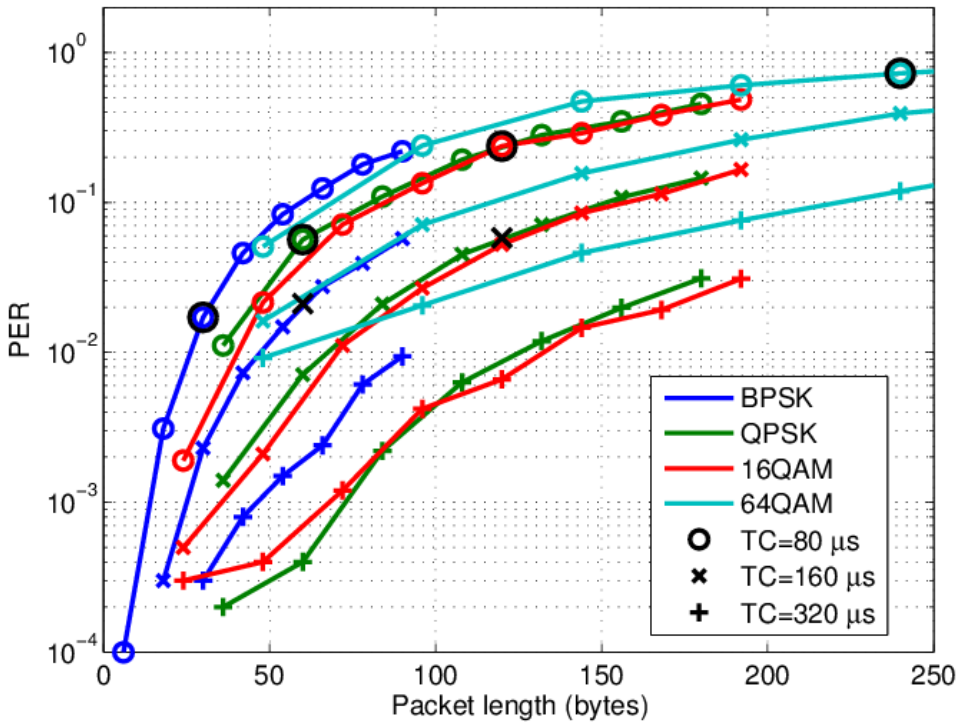

Figure 3.1: Packet error rate versus packet length. Bold dark symbols mark the packet length in bytes whose packet duration is equal to T_C. T_C=320 μs is beyond the plot domain.

cyclic prefix to avoid inter-symbol interference (ISI) regardless of the signal bandwidth, analysis in this chapter utilizes results for the shortest channel (equivalently the largest B_C=7.5 MHz) only. Error performance over channels with smaller B_C was actually upper-bounded by the performance at the largest B_C. In other words, the results presented can be interpreted as worst case results (of the channels simulated). Because the standard has channel coding across subcarriers, increased frequency-domain diversity results in greater coding gain. Unless otherwise stated signal bandwidth is 10 MHz.

Figure 3.1 shows the packet error rate versus packet length for each modulation and several coherence times. Conventional coherence time analysis would predict PER to be 1 for packets whose duration exceeded the coherence time (demarcated by the bold marks). However, the figure shows a gradual increase in error rate. In fact, for a particular coherence time, say 80 μs, the PER of QPSK and 16QAM modulated packets longer than the coherence time is less than

the PER for 64QAM (and BPSK) whose packet are all shorter than the coherence time. This violates conventional coherence time analysis.

This suggests a tradeoff between modulation order (hence, constellation density or minimum inter-symbol distance) and packet duration. While high order modulations result in shorter packets and thus accumulate less channel estimation error, their dense constellations are more susceptible to that error. Conversely, low order modulations result in long packets with greater accumulated error, but less sensitivity due to their large minimum symbol distance. The QPSK and 16QAM packets offer the best tradeoff (of the simulated modulations) between packet duration and estimation error sensitivity.

3.3.2 Latency

Link layer latency accounts for delays both at the PHY and medium-access control (MAC) layers. This includes propagation delay, PHY headers, packet duration, MAC delay (e.g. contention-based backoff), and automatic re-transmission of dropped packets. For this analysis we assume the perfect automatic repeat-request (PARQ) MAC model. This simplified model assumes that dropped packets are re-transmitted instantaneously. A constant delay of L_o OFDM symbols is incurred per packet (original or re-transmitted) and represents the total average PHY and MAC overhead. While this model is quite simple it is reasonable for any system with fixed average delays (e.g. TDMA). It also models the transmission of fragmented packets over standard IEEE 802.11 networks utilizing the distributed coordination function (DCF) MAC, ignoring queuing delays. The resulting latency T_L is

$$T_L \triangleq N(L_o + L_p)T_s \tag{3.4}$$

$$N = \arg\min_N F_X(D; p_e, K) \geq 1 - P_M \tag{3.5}$$

$$D = N - K, \quad K = M/L_p R T_s \tag{3.6}$$

where N is the total number of packets transmitted (including those dropped and re-transmitted D) and T_s is the OFDM symbol period (including the cyclic prefix). K is the number of packets required to complete a M bit message sent at PHY rate R bps using packets consisting of L_p

OFDM symbols each. In words, N is the minimum number of packets transmitted to ensure K successful packets are received with probability $1 - P_M$. By computing N according to P_M we explicitly tie the acceptable performance to the reliability constraints. Network analyses like [BT05,SL07] account for network contention but compute only average throughput independent of any constraints.

Random variable X is negative-binomial distributed with cumulative distribution function (CDF) $F_X(\cdot)$ and probability of (packet) error p_e. The negative-binomial distribution gives the probability of D failures before K successes over a series of Bernoulli trials given success rate $q = 1 - p_e$. The CDF is

$$F_X(D;q,K) = I_q(K,D+1) = \frac{B(q;K,D+1)}{B(K,D+1)} \tag{3.7}$$

$$B(q;K,D+1) = \int_0^q t^{K-1}(1-t)^D dt \tag{3.8}$$

where $I_x(a,b)$ is the regularized incomplete beta function. $B(x;a,b)$ (3.8) is the integral form of the incomplete beta function and $B(a,b) = B(1;a,b)$.

For this analysis, the message error rate $P_M = 0.1$ and the message size $M = 8000$ bits. Figure 3.2 plots the results of applying (3.4) and (3.5) to the curves of Figure 3.1.

3.3.3 Throughput

In the final transformation, we invert the link layer latency to obtain an estimate of the link layer throughput

$$R_{LL} \triangleq M/T_L. \tag{3.9}$$

Figure 3.3 shows the latency curves of Figure 3.2 transformed according to (3.9). Particularly for short coherence times, Figure 3.3 shows that there is an optimal packet length selection that maximizes throughput. It also shows that the optimal packet length is dependent on the modulation.

By substituting (3.4) and (3.6) into (3.9), we can express the throughput as

$$R_{LL} = \frac{M}{N(L_p+L_o)T_s} = R\frac{K}{N}\frac{L_p}{L_p+L_o} = R\frac{\rho}{1+\varepsilon} \approx R\rho(1-\varepsilon). \tag{3.10}$$

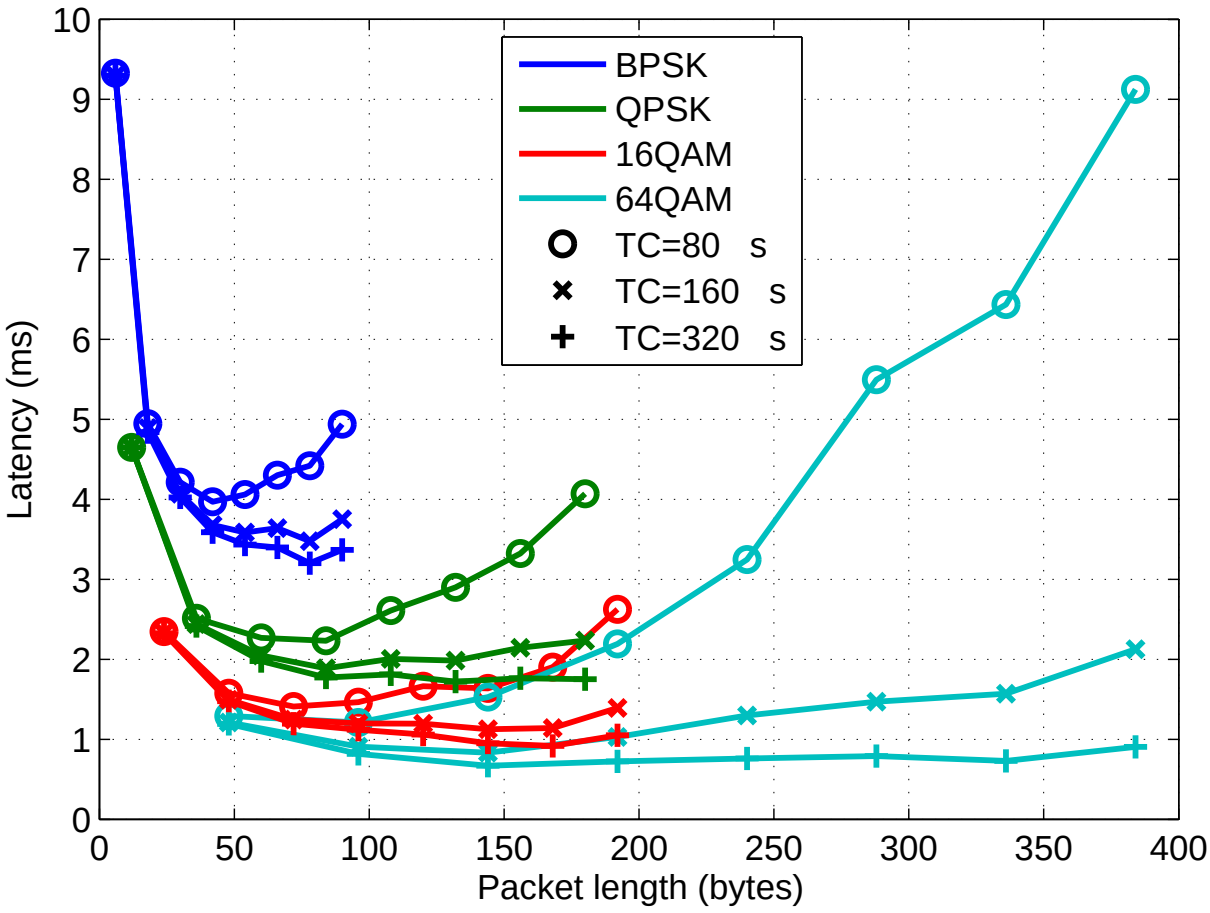

Figure 3.2: Message latency versus packet length.

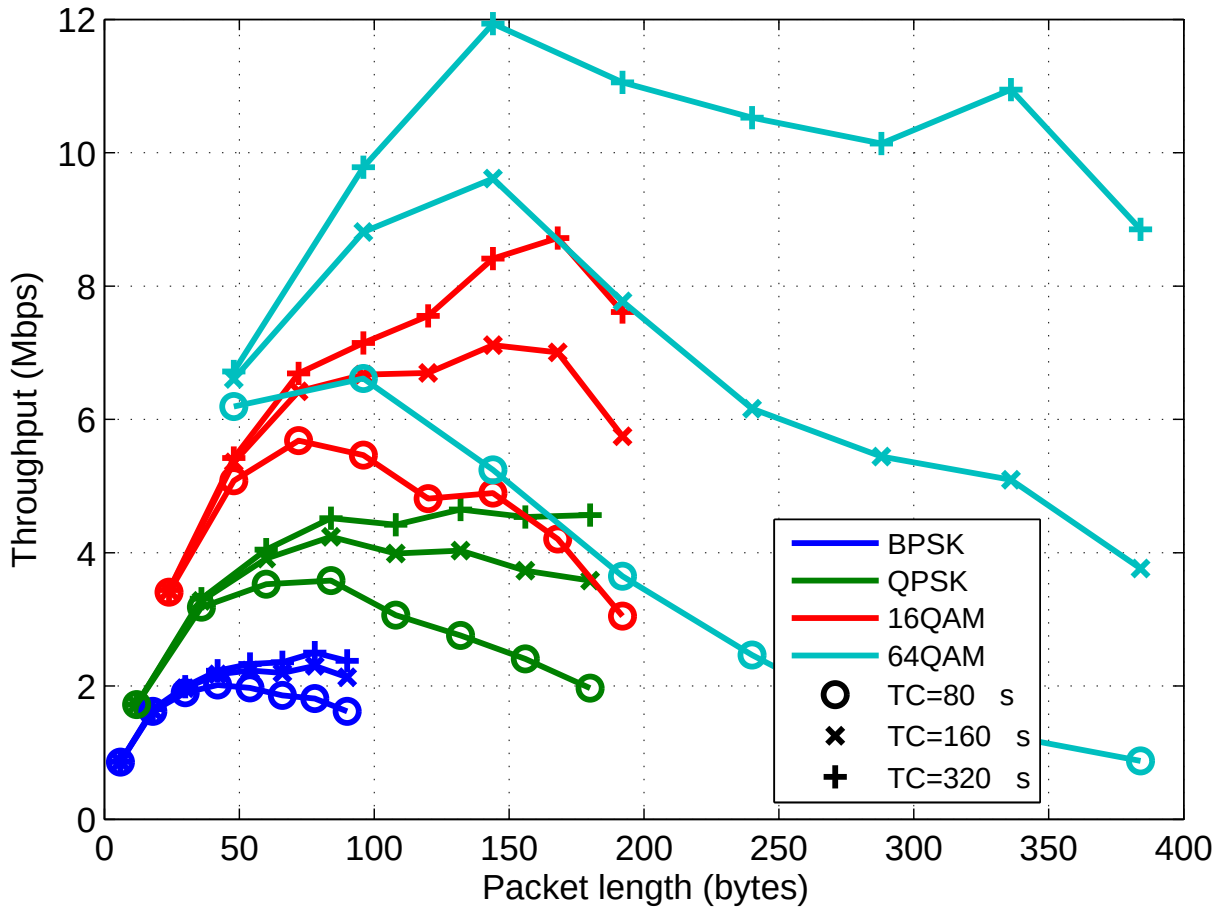

Figure 3.3: Throughput versus packet length.

where $\rho \triangleq K/N$ is the degradation due to re-transmissions and $\varepsilon \triangleq L_o/L_p$ is the degradation due to per packet overhead. The final approximation of (3.10) results from the first-order approximation of $1/(1+\varepsilon)$. Because PER increases with packet length, ε and ρ are inversely related. That is, as packet length increases ε decreases (naturally) while ρ increases. The optimal packet length provides the best tradeoff between the two sources of degradation.

To concisely display results across the range of bandwidths, modulations, packet lengths, and coherence times Figure 3.4 shows a scatter plot of the empirical bandwidth efficiency (β_e) versus normalized coherence time ($\widetilde{T_C}$) where

$$\beta_e \triangleq R\rho/B = \beta\rho \tag{3.11}$$

$$\widetilde{T_C} \triangleq T_C/(RT_sL_p). \tag{3.12}$$

The empirical bandwidth efficiency is the traditional bandwidth efficiency degraded by the overhead of re-transmissions. To isolate this overhead from per-packet overhead the empirical throughput was multiplied by $1/(1+\varepsilon)$ which is equivalent to setting $\varepsilon = 0$ in (3.10).

The plot illustrates trends dependent on modulation and $\widetilde{T_C}$ only. The dashed lines labeled "trad T_C" show the efficiency according to the traditional coherence time, explicitly $\beta I(\widetilde{T_C} > 1)$ where $I(x)$ is the indicator function. The trend lines of Figure 3.4 are the least-square error (LSE) fit to the data of the function

$$f(x) = \frac{v_1}{\frac{v_1}{v_4} + e^{-v_2 x}} + v_3 \tag{3.13}$$

where $\mathbf{v} = \{v_1 \ldots v_4\}$ were determined via an optimization procedure. The function in (3.13) is a generalization of the hyperbolic tangent function, which results by setting $\mathbf{v} = \{2, 2, -1, 2\}$. This function provides a smooth, continuous curve from 0 to a parameterized asymptote, the observed behavior of the bandwidth efficiency.

3.3.4 NETC

Two measures can be computed from the trend line equations. The *plateau* is the bandwidth efficiency achieved for large $\widetilde{T_C}$. Equal to $v_3 + v_4$, the plateau measures the maximum achievable

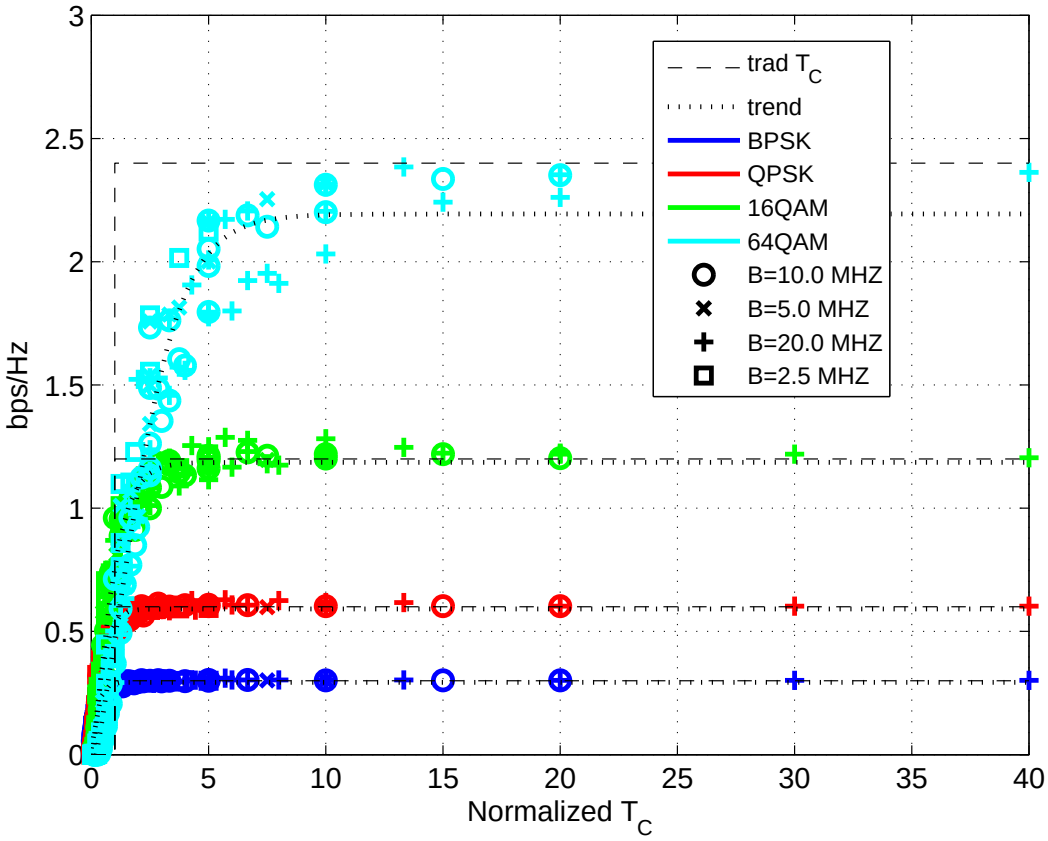

Figure 3.4: Bandwidth efficiency versus normalized channel coherence time.

Table 3.3: Trend Line Parameters, Plateau, And Corner

Modulation	v_1	v_2	v_3	v_4	plateau	corner
BPSK	1.44	4.56	-0.48	0.78	0.29	0.57
QPSK	1.14	3.19	-0.62	1.21	0.59	0.95
16QAM	1.87	1.75	-1.13	2.31	1.18	1.80
64QAM	1.41	0.76	-1.11	3.30	2.20	4.59

performance, i.e. the performance over an effectively static channel. In this region only per-packet overhead ε degrades performance. The *corner* is defined as the normalized coherence time at which we achieve 90% of the plateau performance. The corner is an estimate of the *normalized empirical coherence time (NETC)*. The NETC demarcates the minimum coherence time to packet duration ratio above which the channel impact on performance is considered negligible. Table 3.3 summarizes the optimized parameter sets for the trend lines of Figure 3.4.

Analytically, the plateau should occur at $\lim_{\rho\to 1}\beta_e = \beta$, the underlying PHY efficiencies 0.3, 0.6, 1.2, and 2.4 bps/Hz for BPSK, QPSK, 16QAM, and 64QAM modulations respectively. The plateaus in Table 3.3 generally agree with the expected values except for 64QAM. The plateau is underestimated due to the uniform error weighting across the domain and the paucity of points at high $\widetilde{T}_C$ (in Figure 3.4 the right most data points for 64QAM achieve 2.4 bps/Hz). This would also result in an underestimate of the NETC. The NETC (corner in Table 3.3) varies significantly with modulation. For BPSK and QPSK one can even achieve acceptable performance with a packet duration greater than the traditional channel coherence time. A similar metric based on the traditional channel coherence time would correspond to 1 for all modulations.

3.4 Discussion

Equation (3.13) and Table 3.3 were used to create a parametric approximation for Figure 3.3. The "fit" curves provide a smooth inter/extrapolation of the simulation results while providing a means of generating similar throughput versus packet length curves for a larger set of channels (not simulated). Figure 3.5 shows the synthesized curves along with simulation results extended to large packets for CC $T_C = 320\mu$s, $B_C = 7.5$ MHz. For comparison, a similar transformation was performed using the "trad TC" function of Figure 3.4. The circles mark the packet lengths corresponding to the traditional coherence time. The squares mark the maximum packet length according to the NETC. The "fit" curves capture the major features of the simulated behavior while the "trad TC" curves diverge for longer packet lengths. As mentioned in the previous paragraph, the NETC for 64QAM is underestimated. For each of the other modulations, the NETC packet length is slightly greater than that corresponding to the peak throughput. This is a consequence of our allowance of 10% degradation in our determination of the NETC.

These parametrized curves facilitate generation of results for a wider range of $\widetilde{T}_C$ with greater resolution. Since (3.13) is a function of normalized, not absolute, coherence time, the NETC is applicable to the entire class of channels with the scattering function detailed in Subsection 3.2.2, but with a scaled Doppler spread. This may be particularly applicable to the vehicular scenario where the scattering function is highly dependent on the geography while the Doppler spread is a function of the speed of traffic.

To ascertain the applicability of the canonical channel results to non-canonical channels, Figure 3.6 plots throughput versus packet length from simulations of the GEC and parametrized curves using (3.13). For all curves $T_C = 65$ symbols. The parametrized curves only approximate the optimal packet length. They also provide a loose upper bound on the achievable throughput at higher packet lengths. These inaccuracies would suggest that the fine structure of the channel scattering function has an impact on the actual performance beyond their affect on the coherence time and coherence bandwidth measures.

Despite the error between the "fit" curves and the simulation results, the packet lengths cor-

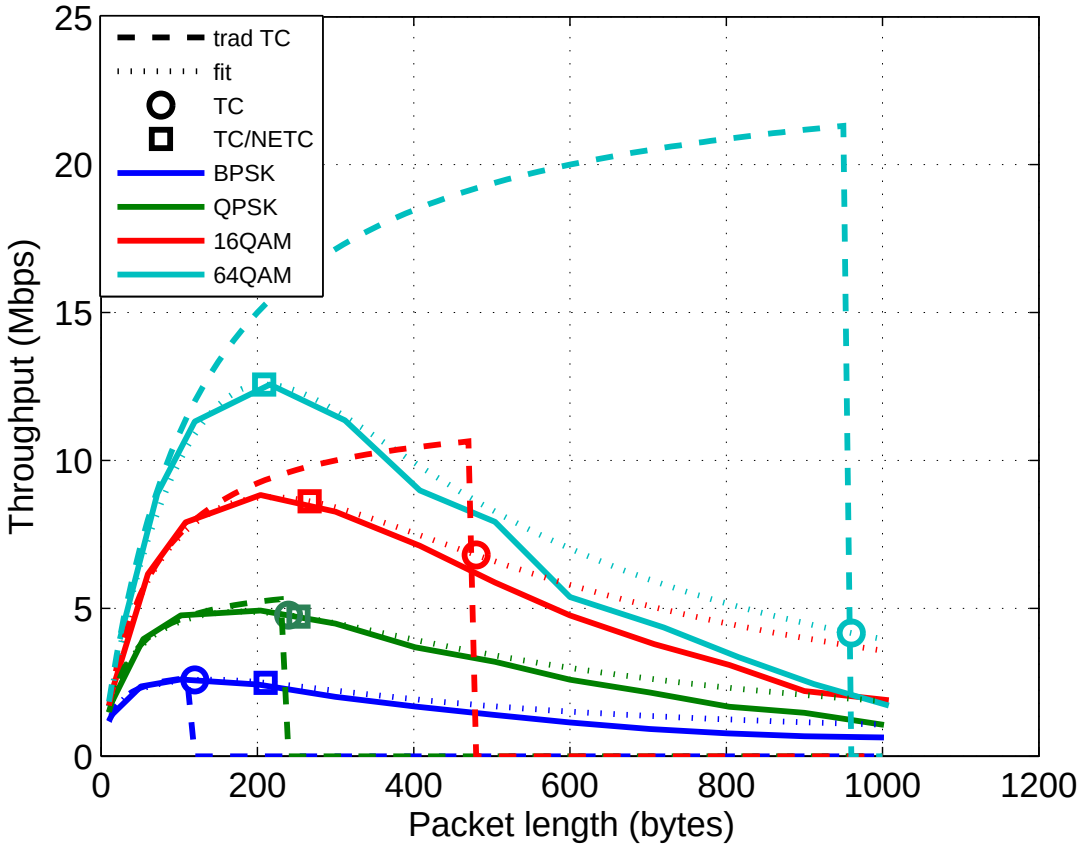

Figure 3.5: Throughput versus packet length for T_C=320 μs.

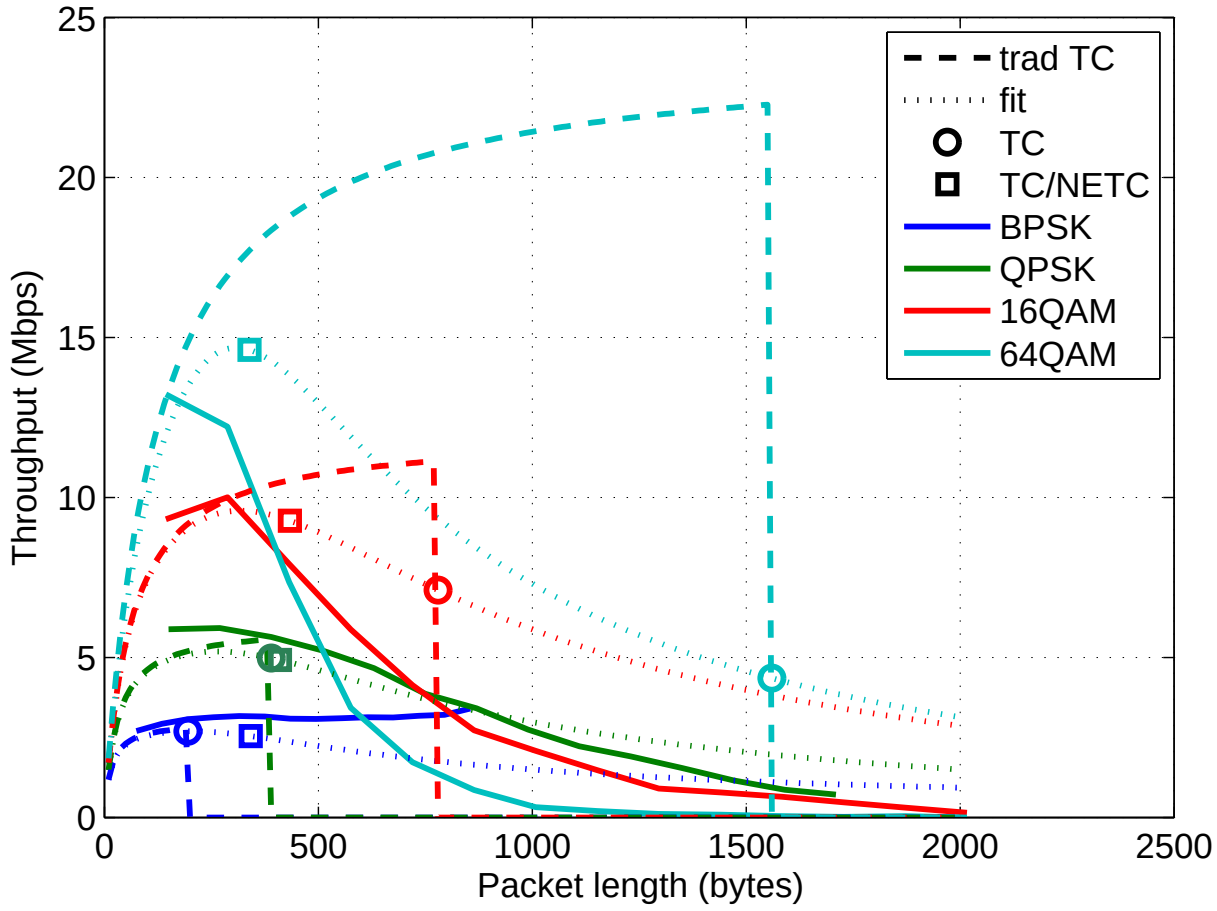

Figure 3.6: Throughput versus packet length for GEC channel T_C=520 μs and B_C ≈4.2 MHz.

responding to the NETC (squares) provides a better bound with which to guarantee throughput performance than does the traditional coherence time (circles). Table 3.4 shows the maximum packet length using the NETC and the throughput maximizing packet length from simulation for two signal bandwidths. The NETC provides a much better guide than does the traditional coherence time of 65 symbols.

3.5 Conclusion

This chapter defined and derived the normalized empirical coherence time which indicates the maximum coherence time (normalized to packet length) necessary to ensure negligible degradation of the link layer throughput of a typical IEEE 802.11p system operating over a time-

Table 3.4: NETC/TC And Simulated Optimal Packet Length (Symbols) And (Simulated) Throughput For The GEC Channel

	B=10 MHz			B=5 MHz		
Modulation	NETC/TC	Sim	Mbps	NETC/TC	Sim	Mbps
BPSK	114	105	3.2	57	45	1.3
QPSK	68	45	5.9	34	25	2.4
16QAM	36	24	10	18	12	3.7
64QAM	14	6	13.2	7	6	4.3

varying channel. Given a fixed channel with a particular coherence time, the NETC was shown to provide a more accurate bound, compared to the traditional coherence time, on the maximum packet length resulting in negligible throughput degradation. While the metric is based on a particular packet, receiver, and channel structure, the NETC provides better guidance than the traditional coherence time in general channels.

For network simulations assuming a non-tracking IEEE 802.11p receiver, the NETC should be used to guide the maximum packet length for which only per-packet overhead impacts throughput. In other words, simulations that assume increasing packet length decreases overhead and thus increases throughput should limit their maximum packet length according to the NETC to maintain valid assumptions. This could have particular impact on network aggregation or coding schemes that rely on large packets.

Future work will quantify those channel parameters that most influence upper layer performance. The impact of alternative signal and receiver structures will also be explored. The goal is to link the signal, channel, and receiver parameter sets to upper layer performance. Such a relationship could provide much needed detail to VANET simulations for network-wide performance evaluation.

CHAPTER 4

Channel Estimation, Overhead, and Outage for PSAM-OFDM

4.1 Introduction

The physical layer (PHY) and medium access control layer (MAC) together define the point-to-point access protocol for communications devices. The PHY provides access to the physical communications channel, wired or wireless, while the MAC manages multi-user coordination, possibly rate adaptation (if the PHY supports it), and some form of error management. Generally in modern systems, the MAC offers at least error detection and basic automatic repeat-request (ARQ) where, upon detecting a packet error, a short message is sent to the packet source requesting a re-transmission. The most efficient communication results from the optimization of this joint model.

This chapter considers the joint design of a pilot symbol-assisted modulation (PSAM) PHY with an ARQ MAC. PSAM provides pilots embedded in the data transmission that are known to the receiver and facilitate channel estimation. Use of PSAM at the PHY holds its own tradeoff: pilots reduce the proportion of the channel access available for data while increasing the achievable rate of the data that is transmitted. This tradeoff has been studied extensively in the literature [HH03, OG02a, OG04, APW09, Loz08]. Each of these investigations optimized the pilot structure to maximize the mean (ergodic) achievable mutual information (MI) at the PHY.

In this investigation, the optimization criterion is *goodput*, a MAC layer metric which accounts for both the overhead of pilots in the PHY and re-transmission of lost packets. The analysis is based on a characterization of the instantaneous mutual information of a PSAM system

operating over a random, selective channel by its mean and variance. The MI variance accounts for channel induced correlation between symbols in the transmitted packet. The simpler mean MI neglects these correlations. The exact MI variance for a non-PSAM system operating over a correlated channel was derived in [MSS08].

The first contribution of this chapter is the characterization of the instantaneous MI variance for a PSAM PHY as a function of the number of pilots, packet length, and channel model parameters. The second contribution uses this result to compute the outage probability as it varies with the PHY pilot design and channel model. We consider a PSAM orthogonal frequency division multiplexing (OFDM) PHY with a fixed number of sub-carriers operating over a multipath channel of known length. Using the MI variance results, we show how to optimize the signal bandwidth (equivalently sub-carrier separation) to maximize the goodput (per unit bandwidth). When the pilot and data powers are not constrained to be equal, we show that the optimum power allocation that maximizes the PHY rate [OG04] also maximizes the goodput. Hence, only the mean MI need be considered when optimizing pilot power.

Section Section 4.2 summarizes previous results utilized in this chapter. Section Section 4.3 describes the system model, section Section 4.4 describes the analysis, Section 4.5 offers results and discussion, and section Section 4.6 offers some conclusions.

4.2 Background

In the ideal receiver all observations, be they training or data, would be used to decode the symbol. The mutual information between N length input vector $\mathbf{x}$ and (possibly larger) output vector $\mathbf{y}$ would be

$$\lim_{N\to\infty} \frac{1}{N} I\left(\mathbf{x}; \mathbf{y}_{\mathcal{D}} | \mathbf{x}_{\mathcal{P}}, \mathbf{y}_{\mathcal{P}}\right), \tag{4.1}$$

where $\mathbf{y}_{\mathcal{A}}$ is the sub-vector made up of elements whose indices are in the set $\mathcal{A}$ and $\mathcal{D}$ and $\mathcal{P}$ are the (disjoint) sets of data and pilot indices, respectively. Decoders that can achieve (4.1) must perform joint channel estimation and data decoding. Most practical systems, however, perform channel estimation and minimum-distance data decoding separately. Though sub-optimal,

this receiver has reduced complexity and makes system analysis tractable. The system model commonly used to describe the observations of this practical receiver is

$$\mathbf{y} = \widehat{\mathbf{H}}\mathbf{x} + \widetilde{\mathbf{H}}\mathbf{x} + \mathbf{w}, \tag{4.2}$$

where $\mathbf{y}$ and $\mathbf{x}$ should be understood to refer only to the data observations, the estimated channel state information (ECSI) $\widehat{\mathbf{H}}$ is derived from the observations $\mathbf{y}_{\mathcal{P}}$, $\widetilde{\mathbf{H}} = \mathbf{H} - \widehat{\mathbf{H}}$ is the channel estimation error of random channel $\mathbf{H}$, and $\mathbf{w}$ is additive white Gaussian noise (AWGN). This model describes the observation of the input through a known channel $\widehat{\mathbf{H}}$ corrupted by additive noise $\mathbf{n} = \widetilde{\mathbf{H}}\mathbf{x} + \mathbf{w}$ that is possibly non-Gaussian and correlated to the first term on the rhs of (4.2). However, if the receiver makes minimum mean square error (MMSE) estimates of the channel it has been shown that the mutual information is lower bounded by the system with independent, identically distributed (IID) Gaussian inputs and $\mathbf{n}$ AWGN, uncorrelated with $\widehat{\mathbf{H}}\mathbf{x}$, with the equivalent noise power [HH03, M00].

This result was used to optimize the number and power of pilots to maximize the ergodic PHY throughput accounting for training overhead, for multi-antenna (MIMO) systems in block fading [HH03], single-antenna narrowband systems in continuous fading [OG02a, Loz08], and wideband OFDM in frequency-selective fading [OG02b, OG04]. Each of these papers focused on maximizing the PHY MI according to the system parameters whereas in this chapter we are interested in goodput. Because the MI distribution of PSAM-OFDM[1] can be well approximated as Gaussian [MSS08], the aforementioned references are optimizing for an outage rate of 50%. We will see that this is far from optimal using the goodput criterion.

The goodput of coded transmissions with ARQ over block fading channels with perfect channel state information (PCSI) at the receiver was considered in [WJ11]. Over a range of signal-to-noise ratios (SNR) the goodput maximizing PHY rate corresponded to an outage probability of approximately 10%. Consequently, the authors suggested resources (e.g. cost and complexity) could be saved by relaxing requirements on the PHY coding rate. In this chapter, we perform a similar analysis but add the effect of pilot overhead on the PHY rate, its impact on

[1] The framework described in this chapter can be applied to any vector transmission satisfying the system assumptions. We take PSAM-OFDM as an illustrative example.

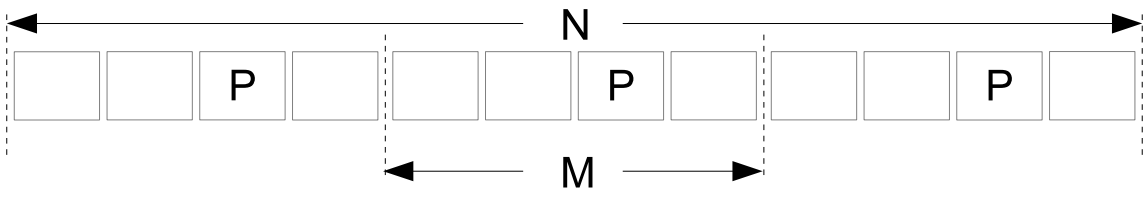

Figure 4.1: Illustration of OFDM block with $M = 4$, $K = 3$, $N = 12$ in the frequency domain. Pilot sub-carriers are marked with a "P".

the MI variance, and compute the statistics for a continuous fading channel rather than a block fading channel.

4.3 System Model

Consider a PSAM-OFDM system transmitting a vector made up of K concatenated sub-vectors each with $M-1$ data symbols and a single pilot at some fixed offset within the sub-block (see Figure 4.1). The total number of data symbols is $|\mathcal{D}| = K(M-1) = N-K$. After transformation to the time-domain via a N point inverse discrete Fourier transform (IDFT),a cyclic prefix (CP) of length L is added and the symbols are sent over a $\bar{L} \triangleq L+1 \leq K$ tap, quasi-static, Rayleigh channel. After removing the CP and demodulating with a DFT, the receiver estimates the channel for $N-K$ data symbols from the K pilots and decodes the data as described in Section 4.2. The receiver observations are expressed by (4.2). Because the pilots are orthogonal to the data and uniformly-spaced cyclically in the OFDM symbol, the achievable mutual information can be expressed as [OG04]

$$I_N = \frac{1}{N} \sum_{n \in \mathcal{D}} \mathsf{E}\left[\log\left(1+\gamma_e |g_n|^2\right)\right], \tag{4.3}$$

where $\mathsf{E}[\cdot]$ is the expectation operator, vector $\mathbf{g} = [g_1, \ldots, g_N] \sim \mathcal{N}_{\mathcal{C}}(\mathbf{0}, R_g)$ is a zero-mean Normal random vector with covariance R_g and $\mathsf{E}[|g_n|^2] = \mathsf{E}[|g|^2] = 1 \,\forall n$, and

$$\gamma_e = \frac{\alpha\gamma(1-\tilde{\sigma}^2_{\Delta h})}{1+\alpha\gamma\tilde{\sigma}^2_{\Delta h}} \tag{4.4}$$

is the effective SNR where α is the proportion of transmit power P devoted to the data, γ is the received SNR, and the channel state information error (CSIE) depends on the channel power-delay profile (PDP) as

$$\tilde{\sigma}^2_{\Delta h} = \sum_{\ell=0}^{L} \frac{\tilde{\sigma}^2_{h_\ell}}{1+(1-\alpha)\gamma\tilde{\sigma}^2_{h_\ell}}, \tag{4.5}$$

where channel tap h_ℓ has power $\sigma^2_{h_\ell}$ and normalized powers $\tilde{\sigma}_i{}^2 = \sigma_i^2/\sigma_h^2$ where $\sigma_h^2 = \sum_{\ell=0}^{L}\sigma^2_{h_\ell}$ is the total channel power.

The PHY model Figure 4.1 is an important bounding case as it results in the minimum average channel estimation error [OG02b, OG04]. It also greatly simplifies analysis. In particular, without such a repeated sub-block structure, γ_e would be dependent on each symbol in the packet [APW09, MM01]. The resulting expressions for the MI mean and variance could still be computed, albeit with much more computational effort, and simplifications like (4.6) and (5.6) would not be possible.

4.4 Analysis

4.4.1 OFDM Outage

The distribution of the mutual information of OFDM with perfect CSI (PCSI), i.e. I_N (4.3) with $\mathcal{D} = \{1 \ldots N\}$, over a frequency-selective channel with AWGN can be accurately approximated as Gaussian at moderate to high SNR ($\gamma > 0\,\text{dB}$) [MSS08]. Modifying [MSS08, eq. 48] for $|\mathcal{D}| = N - K$ data sub-carriers out of N total sub-carriers, and substituting the effective SNR (4.4) the mean mutual information is

$$\mu_I \triangleq \mathsf{E}[I_N] = b_e \frac{N-K}{N}\mathsf{E}[\log(1+\gamma_e|g|^2] = b_e \frac{N-K}{N} e^{1/\gamma_e}\,\mathrm{E}_1(1/\gamma_e), \tag{4.6}$$

where $b_e = \log_2(e)$ converts the expression to bits (from nats). Extending the variance expression [MSS08, eq. 22, 23] accordingly we get

$$\sigma_I^2 \triangleq \mathrm{var}[I_N] = \left(b_e \frac{N-K}{N}\right)^2 \left(\frac{1}{N-K}\varphi(1) - \varphi(0) + \frac{1}{(N-K)^2}\sum_{k\in\mathcal{D}}\sum_{\substack{\ell\in\mathcal{D}\\ \ell\neq k}} \varphi(\rho_d)\right) \tag{4.7}$$

where var[·] is the variance operator, $d = |k-\ell| \in 0 \ldots N-1$ is the sub-carrier separation, and

$$\varphi(\rho_d) \triangleq \begin{cases} e^{2/\gamma_e}\,\mathrm{E}_1{}^2(1/\gamma_e), & |\rho_d| = 0, \\ 2\frac{e^{1/\gamma_e}}{\gamma_e}\,\mathrm{G}_{3,4}^{3,0}(\frac{1}{\gamma_e}|_{0,-1,-1,-1}^{0,0,0}), & |\rho_d| = 1, \\ r_d e^{\frac{2}{\gamma_e r_d}} \sum_{t=0}^{\infty} |\rho_d|^{2t} g_{t+1}^2\left(\frac{1}{\gamma_e r_d}\right), & \text{otherwise}, \end{cases} \tag{4.8}$$

where $g_n(x) \triangleq \sum_{j=1}^{n} \mathrm{E_j}(x)$, $\rho_d = \sum_{\ell=0}^{L-1} \tilde{\sigma}_{h_\ell}^2 e^{-j2\pi d\ell/N} \in [-1,1]$ is the correlation coefficient of the channel between two sub-carriers separated by d indices, $r_d = 1-|\rho_d|^2$, $\mathrm{E}_j(x)$ is the E_n function [AS72, eq. 5.1.4], and $\mathrm{G}_{\mathrm{p,q}}^{\mathrm{m,n}}(x|\cdot)$ is the Meijer-G function [dlm12].

4.4.2 Goodput

We assume independent (re-)transmissions at the MAC layer. This is reasonable considering the MAC must often introduce delays to coordinate access to the channel of multiple users. Modeling such delays is a rich research topic in itself and is beyond the scope of this investigation. The goodput derived in the sequel can be interpreted as the maximum potential goodput neglecting medium access delays.

Let $p_{out}(R)$ be the probability of a failed transmission sent at rate R. The long-term average effective throughput (i.e. goodput) is [WJ11]

$$R_2 \triangleq R_1(1-p_{out}(R_1)) \tag{4.9}$$

where R_1 is the PHY rate. Equivalently, we could define goodput in terms of independent parameter p_{out} and the corresponding PHY rate $R(p_{out})$. If the probability density function (PDF) of the mutual information is Gaussian with mean μ and variance σ^2, then the optimal outage probability that maximizes (4.9) is [WJ11]

$$p_{out}^* \triangleq \arg\max_{p_{out}} (1-\kappa Q^{-1}(p_{out})(1-p_{out}) \tag{4.10}$$

where $Q^{-1}(\cdot)$ is the inverse of the Gaussian tail function and $\kappa \propto \frac{\sigma}{\mu}$, and p_{out} is the independent parameter to be optimized. The optimal outage probability p_{out}^* was shown to be an increasing function of κ [WJ11].

If R is the data rate of the set of M data sub-carriers, the PHY throughput $R_1 = \varepsilon_B R$ where $\varepsilon_B \triangleq \varepsilon_F \varepsilon_T = \frac{N-K}{N+L}$ is the bandwidth efficiency, where $\varepsilon_F \triangleq \frac{N-K}{N}$ and $\varepsilon_T \triangleq \frac{N}{N+L}$ are the frequency and time domain overhead ratios, respectively. Assuming Gaussian MI, the outage probability for R_1 is

$$p_{out}(R_1) = \Phi\left(\frac{R_1}{\varepsilon_B \sigma_I} - \frac{\mu_I}{\varepsilon_F \sigma_I}\right) = \Phi\left(\frac{R_1 - \varepsilon_T \mu_I}{\varepsilon_B \sigma_I}\right) \tag{4.11}$$

where $\Phi(x)$ is the standard Gaussian cumulative distribution function (CDF) and we have accounted for the factor ε_F in μ_I (4.6). It was observed that κ, computed with (4.6) and (5.6) decreased with SNR. Hence, p^*_{out} is also a decreasing function of SNR.

4.5 Results and Discussion

For all results, unless stated otherwise, we assume $N = 64$, K pilots are inserted symmetrically in each OFDM symbol (i.e. pilot offset = $N/2K$), and $\gamma = 20\,\text{dB}$. Pilots and data have equal power, $\alpha = 1 - K/N$. Figure 4.2 shows the outage probability (4.11) versus R_1 with $K = 8$ over a $\bar{L} = 8$ tap channel with an exponentially-decaying PDP with power-decay factor λ, i.e. tap $\ell \in 0 \ldots L$ has gain $\sigma^2_{h_\ell} = e^{-\lambda \ell}$.

The average rate (4.6) increases with γ_e (4.4) which is in turn a decreasing function of λ since, for a fixed pilot set, the CSIE (4.5) decreases as the channel becomes flat. On the other hand, σ^2_I (5.6) is a increasing function of γ_e [MSS08] and, from Figure 4.2, a decreasing function of λ. Intuitively, as λ increases the channel offers greater frequency-diversity and thus less MI variation.

Figure 4.3 shows the outage probability versus R_1 for IID channels of varying length. For each channel the number of pilots $K = \bar{L}$ which maximizes the average rate [OG04]. Unlike the channel power-decay factor, which is a function of the environment, the channel tap length is roughly inversely proportional to the bandwidth of the transmit signal.

Consider the design problem of selecting the channel bandwidth B_C for a scalable 64 sub-carrier PSAM-OFDM system given 16 MHz of available spectrum. Assume the channel PDP is uniformly distributed with maximum excess delay of $1\,\mu s$ such that the sampled PDP is IID

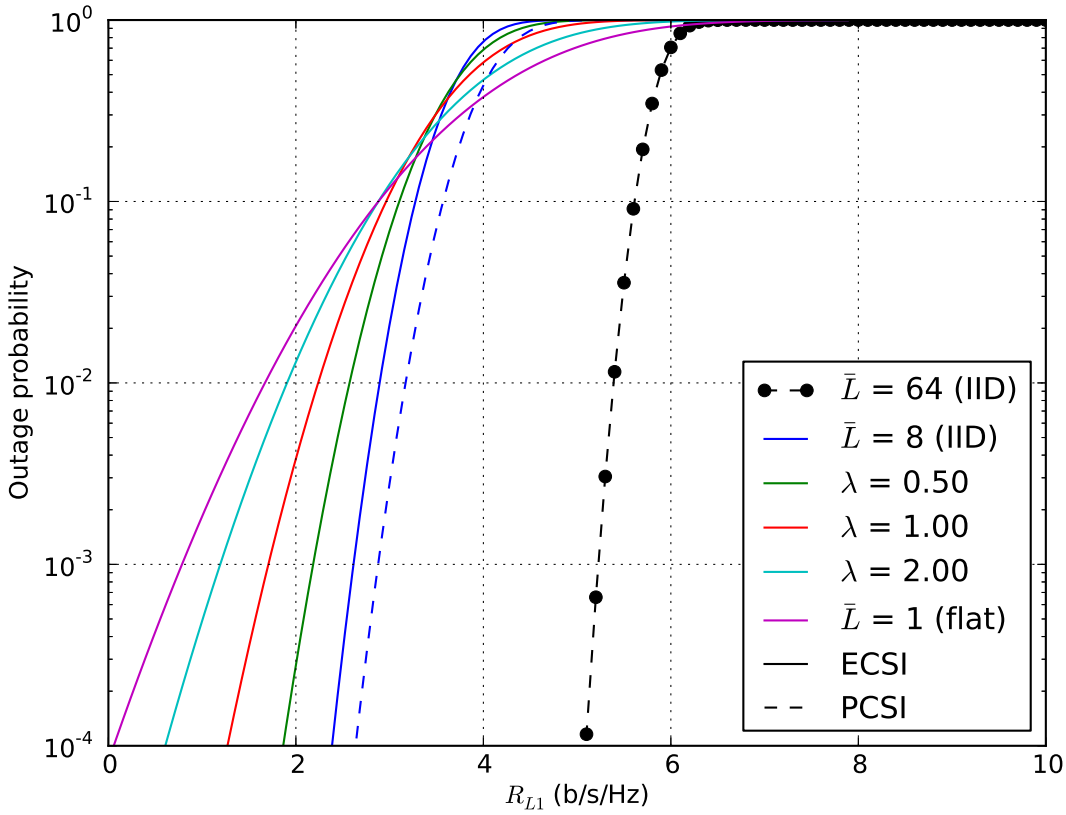

Figure 4.2: Outage probability versus R_1 for $N = 64$, $K = \bar{L} = 8$ over a channel with exponentially-decaying PDP with decay-factor λ. The $\bar{L} = 8$ (IID) and $\bar{L} = 1$ (flat) curves correspond to the limiting cases $\lambda = 0$ and $\lambda = \infty$, respectively. The plain dashed line is $\bar{L} = 8$ (IID) with PCSI. The circle-dashed line $\bar{L} = 64$ (IID) given as an ideal reference is for PCSI, no overhead, and a completely uncorrelated channel.

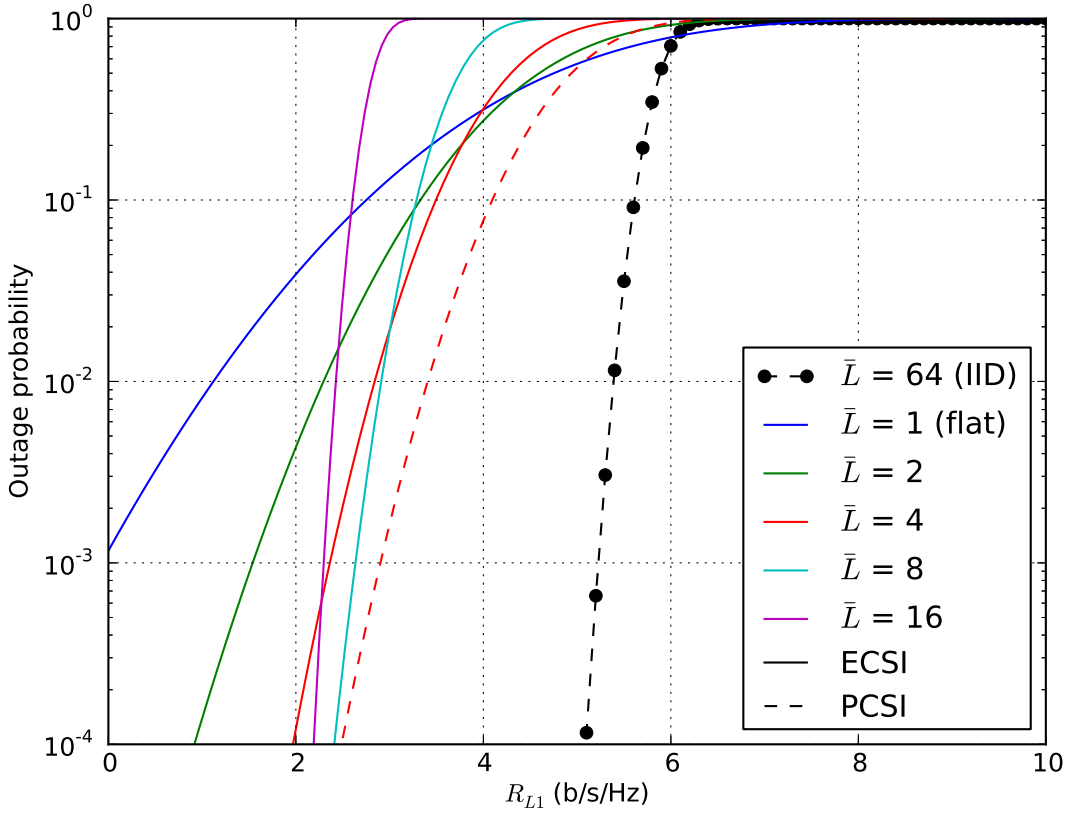

Figure 4.3: Outage probability versus R_1 for $N = 64$ and $K = \bar{L}$ (except for $\bar{L} = 64$ (IID) which is identical to that in Figure 4.2 and neglects overhead altogether) over IID channels of length $\bar{L}$. The plain dashed line is $\bar{L} = 4$ with PCSI.

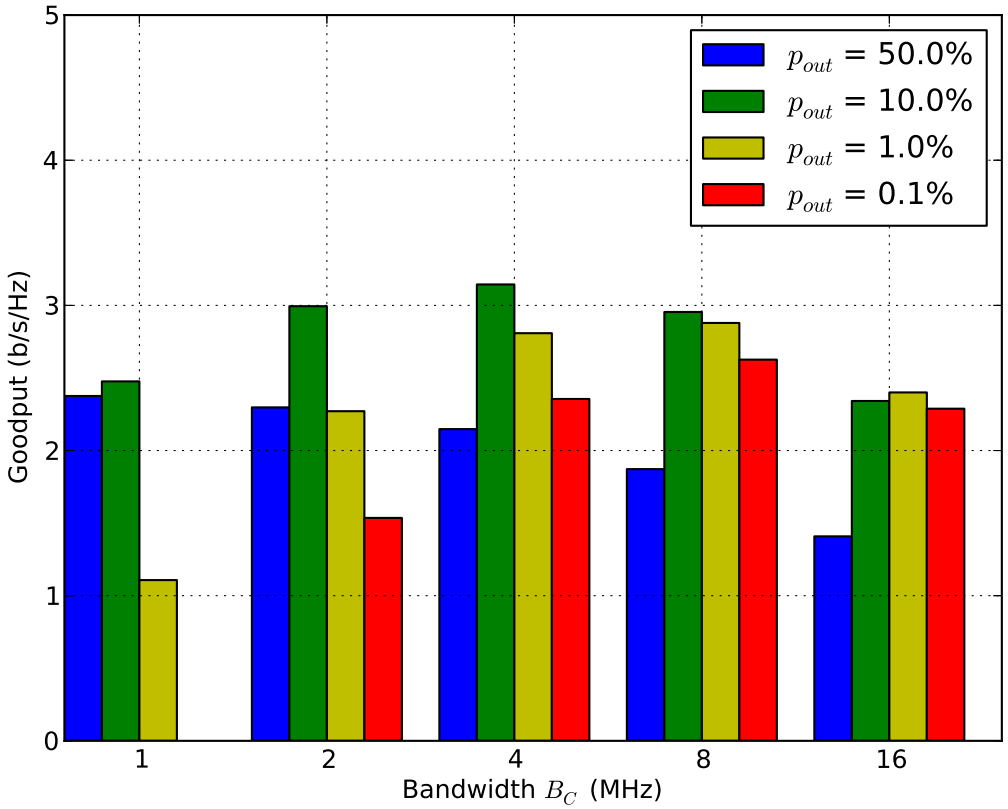

Figure 4.4: Goodput R_2 versus B_C for $N = 64$, $K = \bar{L}$ over IID channels of length $\bar{L} = B_C \times 1\,\mu s$.

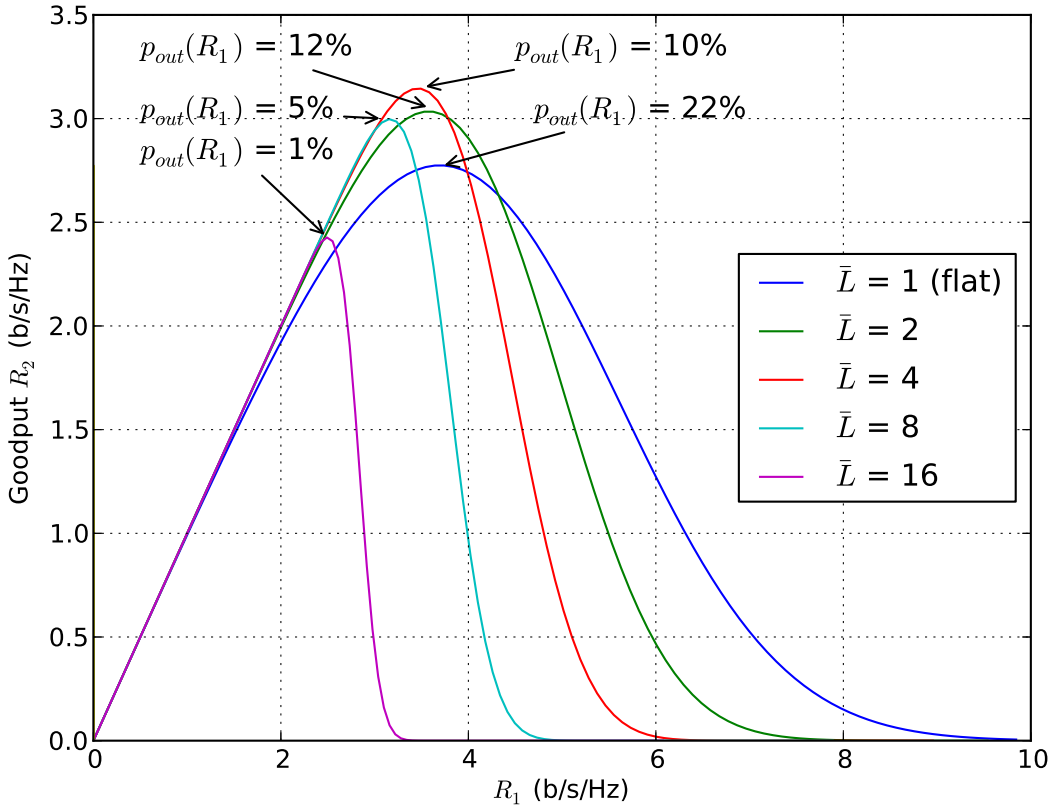

Figure 4.5: Goodput R_2 versus R_1 for $N = 64$, $K = \bar{L}$ over IID channels of length $\bar{L}$.

at up to 16 MHz sampling rate. Targeting 90% availability (equivalently 10% outage), the most efficient use of spectrum according to Figure 4.3 would be over a $\bar{L} = 4$ tap channel which corresponds to a channel bandwidth $B_C = \frac{\bar{L}}{1\mu s} = 4\,\text{MHz}$. This result differs from that which minimizes the MI variance, $B_C = 16\,\text{MHz}$, or that maximizes the average rate, $B_C = 1\,\text{MHz}$. Targeting 99.9% availability, the optimium $B_C = 8\,\text{MHz}$. Figure 4.4 shows the goodput verus bandwidth for this example and several target outage probabilities. Note that the optimal choice of bandwidth depends on the target outage, but that $B_C = 4\,\text{MHz}$ with an outage of about 10% gives the overall maximum goodput.

Figure 4.5 shows the goodput (4.9) computed from the curves of outage probability versus PHY rate of Figure 4.3. The goodput maximizing outage probability marks each peak. The overall goodput maximizing selection corresponds to that whose channel length is $\bar{L} = 4$ with a

corresponding outage rate of about 10%. This result agrees with a similar analysis considering goodput versus coding overhead [WJ11].

When the proportion of power allocated to pilots and data can be tuned, additional optimization can lead to further performance gains [JL10, OG04, HH03]. This chapter approaches the problem from the cross-layer perspective of maximizing R_2. Figure 4.6 shows the R_1, R_2, and p_{out} that maximize R_2 versus the proportion of power allocated to data α, see (4.4). The power allocation affects the MI statistics only through the effective SNR. Since the optimal outage is a decreasing function of SNR (see section Subsection 4.4.2), and the achievable rate R_1 is an increasing function of SNR, maximizing the effective SNR (or equivalently R_1) will also maximize R_2.

The plot marks the allocation α^* that was numerically optimized to maximize goodput. This maximizes R_1, minimizes p_{out} and thus maximizes R_2. Three alternative allocations from [OG04] are included for comparison. These allocations were analytically derived from the channel and signal parameters to maximize R_1. The performance loss between α^* and the alternatives is marginal, thus optimizing for R_1 will yield nearly optimal R_2 performance.

4.6 Conclusion

This chapter investigated the effect of training overhead and the resulting imperfect channel state information on the outage probability and goodput for a PSAM-OFDM PHY paired with a ARQ MAC operating over a quasi-static, Rayleigh multipath channel. We extended expressions for the mean and variance of the mutual information of OFDM systems with no training to those which include pilots.

We identified a tradeoff for outage rate (i.e. the achievable rate at a given outage probability) between increased frequency diversity and the overhead necessary to take advantage of the diversity. This result has implications for deriving channelization (i.e. partitioning a given bandwidth into a number of independent channels) strategies that maximize the overall bandwidth efficiency. Finally we showed that the optimal power allocation to maximize goodput

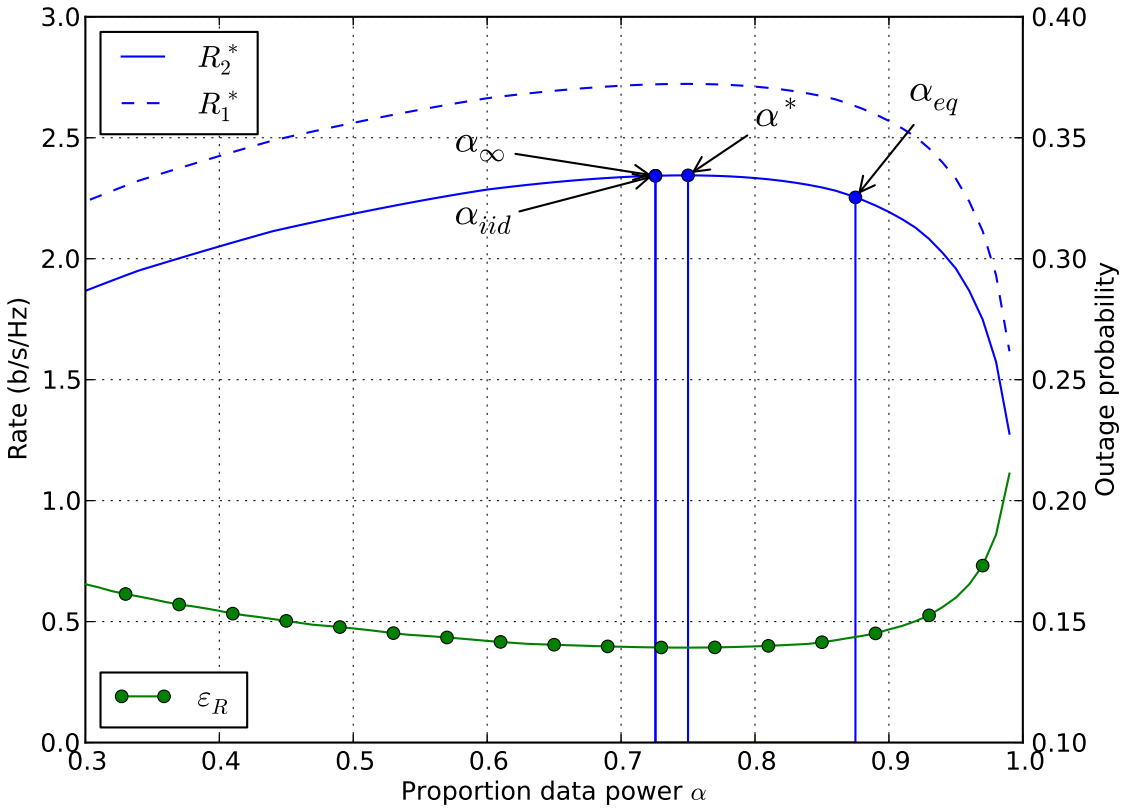

Figure 4.6: Optimal goodput R_2 with the corresponding PHY rate R_1 and outage probability p_{out} versus the proportion of data power α over a channel with exponentially-decaying PDP with $\lambda = 1$. Marked allocations are for a) equal power α_{eq}, b) optimized R_1 at high SNR α_∞, c) optimized R_1 for IID channels α_{iid}, [OG04], and d) optimized R_2 allocation α^*.

was equivalent to that which maximizes the effective SNR and PHY rate.

CHAPTER 5

Analytic Bounds for Mutual Information Variance in Time-Varying Channels

5.1 Introduction

Pilot symbol-assisted modulation (PSAM) is ubiquitous among modern communications standards. PSAM embeds training sequences, or pilots, known at the receiver into a transmitted signal in order to facilitate receiver-side channel estimation. Proper design of PSAM systems balances the loss in data rate due to reserving resources for training and the gains in data rate due to improved channel estimation.

This tradeoff as it affects the mean (ergodic) mutual information has been studied extensively in the literature [HH03, APW09, OG02a, OG04]. However, the impact of pilot design and estimated channel state information (ECSI) on the variance of the mutual information has received less attention. Since the MI distribution of a vector transmission over a correlated Rayleigh fading channel can be well approximated as Gaussian [MSS08, CST07], the MI mean and variance fully characterize the information outage probability. While the mean depends solely on the signal-to-noise ratio (SNR), the MI variance accounts for the channel correlation across the transmitted signal. The majority of prior analyses consider only non-PSAM transmissions ([DF12] excepted) with perfect channel state information (PCSI) and all of the prior analyses require numerical computation of the MI variance from the channel correlation coefficients, offering only limited insight [MSS08, Ass09, CST07].

This chapter (ultimately) considers the MI variance in a PSAM system with ECSI. We present an expression for the exact PSAM MI variance. First considering narrowband non-

PSAM transmissions over time-varying channels with PCSI at the receiver, we derive bounds of the MI variance based on the channel process Doppler spectrum and transmission block length. For the case of a rectangular (flat) Doppler spectrum, these bounds admit an intuitive closed form. The MI variance bounds for the flat spectrum are shown to correspond bound the block fading case. A similar results was presented for the mean MI [JL10]. The non-PSAM PCSI bounds are then modified for PSAM with ECSI under reasonable constraints on the proportion of pilots within the transmission.

5.2 System Model

5.2.1 PCSI

Assuming perfect synchronization, a block of N observations of a narrowband transmission through a correlated (flat) Rayleigh fading channel at the output of the matched filter of the receiver is

$$y(t) = h(t)x(t) + w(t), t = kT_s, k \in [0, N-1], \tag{5.1}$$

where T_s is the symbol period, both w and h are stationary complex zero-mean Gaussian distributed with unit variance $\mathcal{N}_{\mathcal{C}}(0,1)$ and $\gamma = \mathsf{E}[|x|^2]$ is the signal-to-noise ratio (SNR). The processes h, x, and w are mutually independent. The correlation function of h is dictated by its Doppler spectrum $S_H(e^{j\omega})$ where

$$\begin{aligned} S_H(e^{j\omega}) &> 0, \ |\omega| \leq \omega_m \\ S_H(e^{j\omega}) &= 0, \ |\omega| > \omega_m, \end{aligned}$$

where $\omega_m = 2\pi f_m$ and f_m is the maximum Doppler. Thus, in the sequel the correlation coefficient between channel realizations n symbols apart is

$$\begin{aligned} \rho_n &\triangleq \mathsf{E}[h(kT_s)h^*((k+n)T_s)] \\ &= \frac{1}{2\pi}\int_{-\pi}^{\pi} S_H(e^{j\omega})e^{jn\omega}\,\mathrm{d}\,\omega. \end{aligned} \tag{5.2}$$

For the flat (rectangular) Doppler spectrum, substitute

$$S_F(e^{j\omega}) = \begin{cases} \frac{1}{2f_m}, & |\omega| \leq \omega_m \\ 0, & \text{otherwise} \end{cases} \tag{5.3}$$

for $S_H(e^{j\omega})$ in (5.2). The rectangular Doppler spectrum is an important special case since it upper bounds the channel estimation error variance for all Doppler spectra given equal f_m and hence, lower bounds the achievable mean mutual information [JL10].

5.2.2 ECSI

The PSAM system model differs from (5.1) in that we insert a pilot symbol once every M symbols. Let the proportion of pilots be $\alpha = 1/M$ and, for PCSI, $\alpha = 0$. The ECSI signal model is

$$\begin{aligned} y(t) &= \hat{h}(t)x(t) + \Delta h(t)x(t) + w(t) \\ &= \hat{h}(t)x(t) + n(t), t = kT_s, k \in [0, N-1], \end{aligned} \tag{5.4}$$

where $\hat{h}(t)$ and $\Delta h(t)$ are the channel estimate and error at t, respectively. Comparing to (5.1), $h(t) = \hat{h}(t) + \Delta h(t)$. In the final line, $n(t) = \tilde{h}(t)x(t) + w(t)$ is an effective additive noise term that, generally, is not Gaussian nor independent of the signal term $\hat{h}(t)x(t)$. However, if ECSI is obtained via minimum mean-square error (MMSE) channel estimation, $n(t)$ is uncorrelated with the signal term and the mutual information can be lower bounded by a system with Gaussian inputs $x(t)$, known channel $\hat{h}(t)$, and additive white Gaussian noise (AWGN) whose variance is equal to that of $n(t)$ [HH03, M00].

If we further restrict the block size to be $N = KM, K \in \mathcal{N}^+$, the block contains K pilots uniformly distributed in the block and the effective SNR γ_e, accounting for CSI error (CSIE), is uniform across the block. The mutual information in this case is [OG04, OG02a]

$$I_{N,\alpha} = (1-\alpha) \sum_{n \in \mathcal{D}} \log_2(1 + \gamma_e |\hat{h}_n|^2), \tag{5.5}$$

where subscript N on the lhs indicates the block size, $\alpha = 1/M$ is the proportion of pilot symbols in the block, $\mathcal{D}$ is the set of data indices, γ_e depends on the channel, and $\hat{h}_n$ are, in general,

correlated. For PCSI $\alpha = 0$ and the effective SNR is equal to the received SNR, i.e. $\gamma_e = \gamma$, and $\hat{h_n} = h_n$. The constraints on the block size and pilot structure listed above (5.5) are a useful case. As the block length N and pilot count K tend to infinity, this structure maximizes γ_e and thus maximizes the average mutual information, i.e. the mean of (5.5) [OG02a]. We make use of γ_e assuming asymptotically large N in order to simplify the analysis and enable closed form expressions that yield insights into the effect of various parameters. For finite block size and general pilot structure, numerical methods are required to obtain case specific results.

5.3 Analysis

5.3.1 PCSI

The variance of the mutual information of the N-length vector of observations (5.1) is [MSS08]

$$\sigma_I^2 \triangleq \mathrm{var}[I_N] = \frac{b_e^2}{N^2} \sum_{n=-N+1}^{N-1} (N-|n|) f(a_n) - f(0) \tag{5.6}$$

where $\mathrm{var}[\cdot]$ is the variance operator, $b_e = \log_2(e)$ converts from nats to bits, n is the integer symbol separation, and

$$f(a_n) \triangleq \begin{cases} e^{2/\gamma} \mathrm{E}_1{}^2(1/\gamma), & a_n = 0, \\ 2\frac{e^{1/\gamma}}{\gamma} \mathrm{G}_{3,4}^{3,0}\left(\frac{1}{\gamma}\middle|_{0,-1,-1,-1}^{0,0,0}\right), & a_n = 1, \\ r_n e^{\frac{2}{\gamma r_n}} \sum_{t=0}^{\infty} a_n^t g_{t+1}^2 \left(\frac{1}{\gamma r_n}\right), & \text{otherwise}, \end{cases} \tag{5.7}$$

where γ is the signal-to-noise ratio, $g_n(x) \triangleq \sum_{h=0}^{n} \mathrm{E_h}(x)$, $a_n \triangleq |\rho_n|^2 \in [0,1]$, $r_n \triangleq 1 - a_n$, $\mathrm{E}_h(x)$ is the generalized exponential integral function [AS72, eq. 5.1.4], and $\mathrm{G}_{p,q}^{m,n}(x|\cdot)$ is the Meijer-G function [dlm12].

The function $f(a)$ is a convex, though nearly linear, monotonically increasing function of a. Define two linear bounds

$$f(a) \le m_U a + b_U = (f(1) - f(0))a + f(0) \tag{5.8a}$$

$$f(a) \ge m_L a + b_L = (1 - \sqrt{f(0)}/\gamma)^2 a + f(0). \tag{5.8b}$$

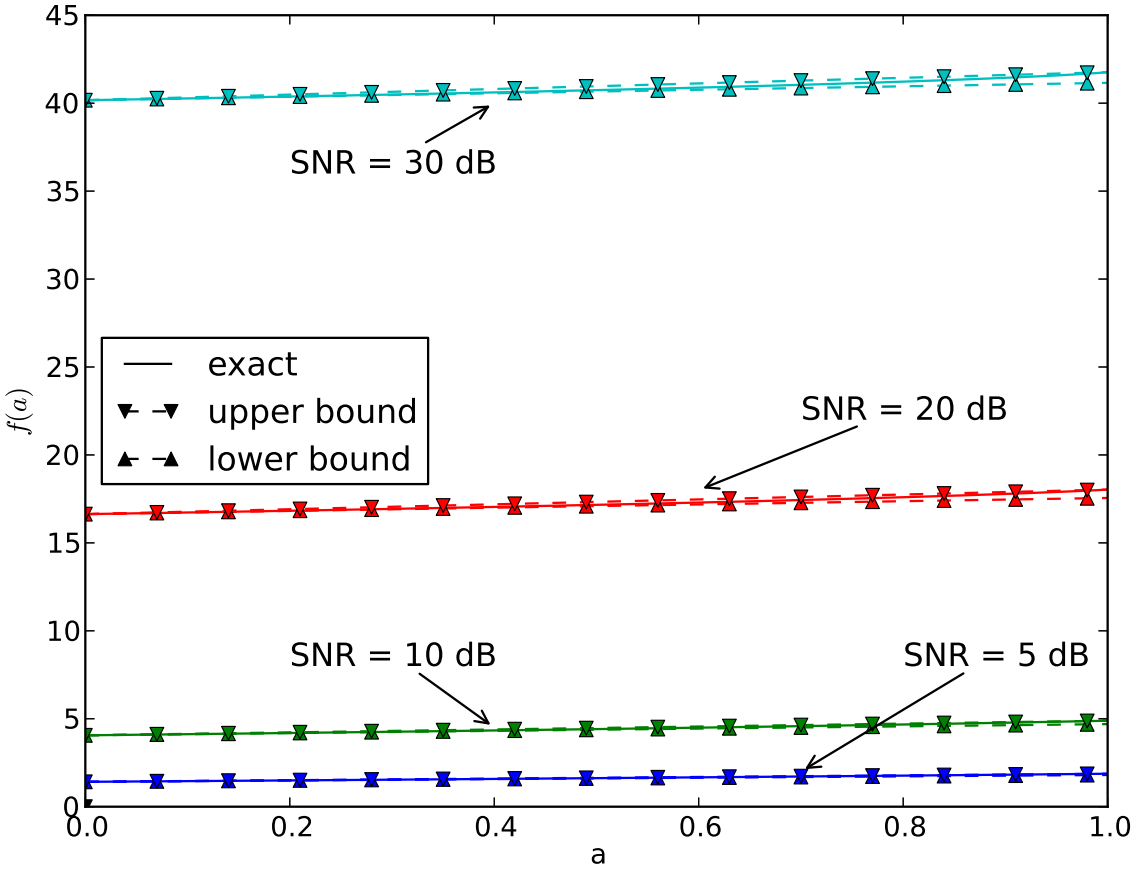

Figure 5.1: Plots of the proposed function $f(a)$ versus argument $a \in [0,1]$. The exact function value is plotted along with linear upper and lower bounds.

Note that $b_U = b_L = b = f(0)$ and $m_U = \text{var}[I_1]/b_e^2$, i.e. it is proportional to the MI variance with a flat channel. The lower bound (5.8b) is the first order Taylor approximation of $f(a)$ about 0. Figure 5.1 shows the function $f(a)$ along with the two bounds for several values of SNR.

Substituting the generic linear function $L(a) = m_X a + \varphi(0)$ as a proxy for each bound in (5.8) into (5.6)

$$\sigma_I^2 \gtreqless b_e^2 m_X \sum_{n=-N+1}^{N-1} w_n a_n = b_e^2 m_X (w * a)(0) = b_e^2 m_X \bar{a} \tag{5.9}$$

$*$ is the convolution operator and

$$\bar{a} \triangleq (w*a)(0) = \frac{1}{2\pi}\int_{-\pi}^{\pi} W(e^{j\omega})(S_H * S_H)(e^{j\omega})\,\mathrm{d}\omega. \tag{5.10}$$

The weighting function is the normalized discrete triangle function

$$w_n = \frac{1}{N}\mathrm{tri}\left(\frac{n}{N}\right) = \begin{cases} \frac{1}{N} - \frac{|n|}{N^2}, & |n| < N \\ 0, & \text{otherwise,} \end{cases} \tag{5.11}$$

whose Fourier transform $W(e^{j\omega}) = \mathrm{sinc}^2(N\omega/2)$ where $\mathrm{sinc}(x) = sin(x)/x$. The value $\bar{a}$ is the weighted average squared-magnitude channel correlation. For general spectra (5.10) must be computed numerically. However, substituting (5.3) in (5.10), $\bar{a}$ can be bounded for $N > 1/2f_m$ by

$$\frac{\pi - 1}{\theta} - O(\theta^{-2}) \leq \bar{a} \leq \frac{\pi}{\theta} + O(\theta^{-3}), \tag{5.12}$$

where $\theta = 2\pi N f_m$. The derivation of these bounds is in Appendix A.1. Substituting these bounds into (5.9), the bounds on the mutual information variance are

$$\sigma_I^2 \leq b_e^2\left(f(1) - f(0)\right)\left(\frac{\pi}{\theta} + O(\theta^{-3})\right) \triangleq \sigma_{UB}^2, \tag{5.13a}$$

$$\sigma_I^2 \geq b_e^2\left(1 - \frac{\sqrt{f(0)}}{\gamma}\right)^2\left(\frac{\pi - 1}{\theta} - O(\theta^{-2})\right) \triangleq \sigma_{LB}^2. \tag{5.13b}$$

In addition to the bounds of (5.13), a simple approximation is proposed consisting of the average of the the two bounds

$$\sigma_A^2 = \frac{\sigma_{LB}^2 + \sigma_{UB}^2}{2} \tag{5.14}$$

While (5.12) groups the asymptotically negligible terms in bounding functions $O(\cdot)$ to highlight the dominant behavior, the exact bounds for $\bar{a}$ (including the asymptotically negligible terms) are used when evaluating (5.13) and (5.14) for all plots.

5.3.2 ECSI

Residual error from channel estimation reduces the effective SNR at the receiver and alters the statistics of the mutual information. The effective SNR accounting for channel estimation error

with variance $\sigma^2_{\Delta h}$ is [OG02a, JL10]

$$\gamma_e \triangleq \frac{\gamma(1-\sigma^2_{\Delta h})}{1+\gamma\sigma^2_{\Delta h}} \tag{5.15}$$

where

$$\sigma^2_{\Delta h} = 1 - \frac{1}{2\pi}\int_{-\pi}^{\pi} \frac{\gamma|S_H(e^{j\omega})|^2}{1/\alpha+\gamma S_H(e^{j\omega})}\,\mathrm{d}\,\omega \tag{5.16}$$

and for the flat spectrum

$$\sigma^2_{\Delta h} = \frac{1}{1+\frac{\alpha}{2f_m}\gamma}. \tag{5.17}$$

The mutual information mean and variance are [DF12]

$$\mu_{I_{N,\alpha}} \triangleq b_e \frac{M-1}{M}\,\mathsf{E}[I_1] = b_e(1-\alpha)e^{1/\gamma_e}\,\mathsf{E}_1(1/\gamma_e) \tag{5.18}$$

$$\sigma^2_{I_{N,\alpha}} \triangleq b_e^2(1-\alpha)^2 \sum_{n=-N+1}^{N-1} w_{n_\alpha} a'_n, \tag{5.19}$$

respectively, where w_{n_α} is the amended ECSI weight function and a'_n is the squared-magnitude of the correlation coefficient of the estimated channel process $\hat{h}(t)$ (5.4).

Figure 5.2 shows the positive half of the symmetric weight functions for $N = 80$. The PCSI weight distribution ($\alpha = 0$) only approximates the ECSI weights, with the approximation improving as the sub-block size M increases. Because the ECSI weights do not admit simple functional expression with a well-defined Fourier transform, we will approximate the ECSI weights by the PCSI weights when computing the bounds for (5.19). To evaluate the exact ECSI variance (5.19) plotted in the figures of Subsection 5.4.2, the exact weights w_{n_α} are used. While the bounds derived in the sequel are shown in to be valid over reasonable ranges of the parameters of interest, they are not guaranteed valid as in the PCSI case because of the approximation of the weight function.

To maximize the mean MI, pilots must be inserted every $M = \lfloor 1/2f_m \rfloor$ [OG02a]. For most practical scenarios, $f_m < 0.1$, thus $M \geq 5$ [JL10].

The spectrum of $\hat{h}(t)$ is the integrand of the term on the rhs of (5.16) [OG02a]

$$S_{\hat{H}}(e^{j\omega}) = \frac{\gamma|S_H(e^{j\omega})|^2}{1/\alpha+\gamma S_H(e^{j\omega})}. \tag{5.20}$$

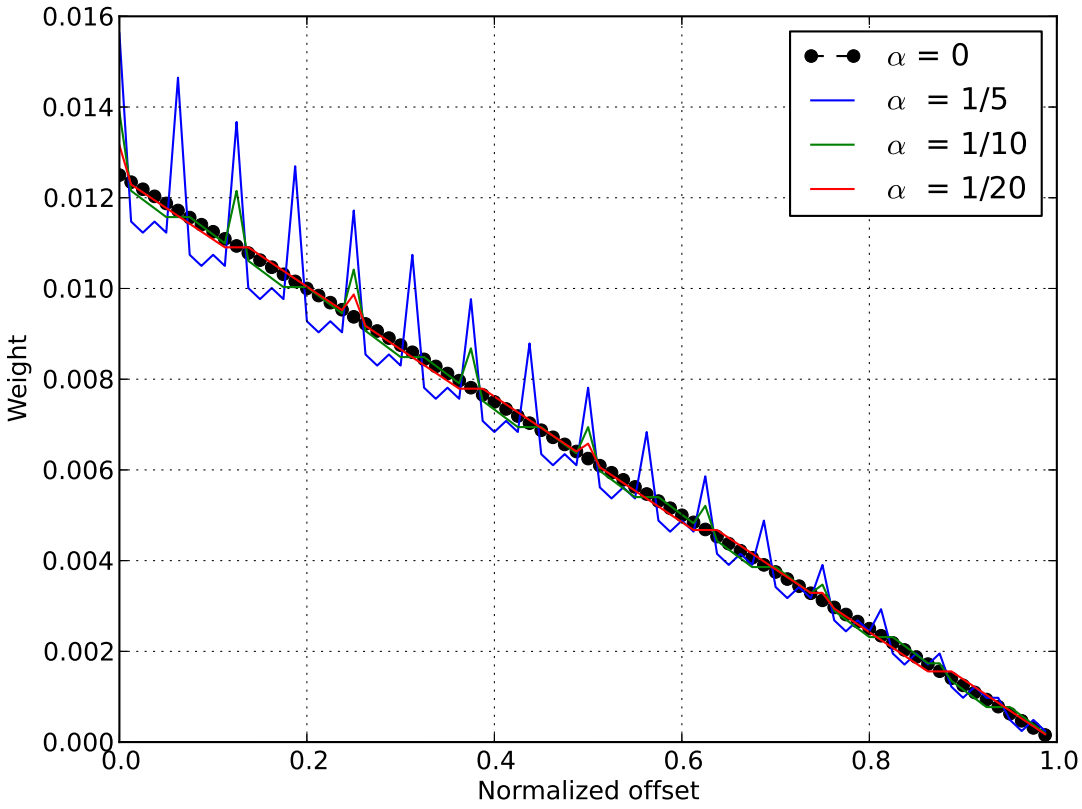

Figure 5.2: Positive half of the weight function w_n for PSAM models with varying α. The x-axis offset index is normalized by the block size $N = 80$.

In general, this function must be computed numerically. However, for the flat Doppler spectrum

$$S_{\hat{F}}(e^{j\omega}) = \frac{1}{\beta} S_F(e^{j\omega}), \tag{5.21}$$

where $\beta = 1 + \frac{2f_m}{\gamma\alpha}$ is just a scalar constant which is normalized out of the correlation coefficient, hence, $a'_n = a_n$ and (5.12) applies.

This gives ECSI variance bounds of

$$\sigma^2_{UB} \geq \frac{\sigma^2_{I_{N,\alpha}}}{(1-\alpha)^2} \geq \sigma^2_{LB} \tag{5.22}$$

Note that the SNR used to compute (5.13a) and (5.13b) in (5.22) is the effective SNR (5.15).

In terms of mean MI, the continuous fading channel with flat Doppler spectrum was shown to be equivalent to the block fading channel with $M = 1/(2f_m)$ [JL10]. Making this substitution in $\pi/\theta = M/N = 1/K$, thus the variance decreases with the number of M length blocks identically to that of a block fading channel. Hence, these bounds suggest the equivalence between these two channels carries over to the MI variance. However, unlike the mean MI, we cannot claim that the MI variance resulting from a flat Doppler spectrum channel bounds the variance for all spectra. Considering other spectra can have power concentrated at the band edges (e.g. Jakes Doppler spectrum) or the band center (e.g. a round spectrum) we conjecture that the flat spectrum does not bound the variance above or below.

5.4 Results and Discussion

For the plots in this section, the block size $N = 80$ symbols and $M = 5$ unless noted otherwise. The variance for curves labeled "PCSI" were computed from (5.6) and (5.7). The statistics of curves labeled "ECSI" were computed using (5.18) with the true weight function w_{n_α} and equations (5.19) and (5.15). Curves labeled "IECSI" (ideal ECSI) correspond to "ECSI" curves with infinite pilot SNR. Thus, for those curves substitute the actual SNR γ in place of γ_e.

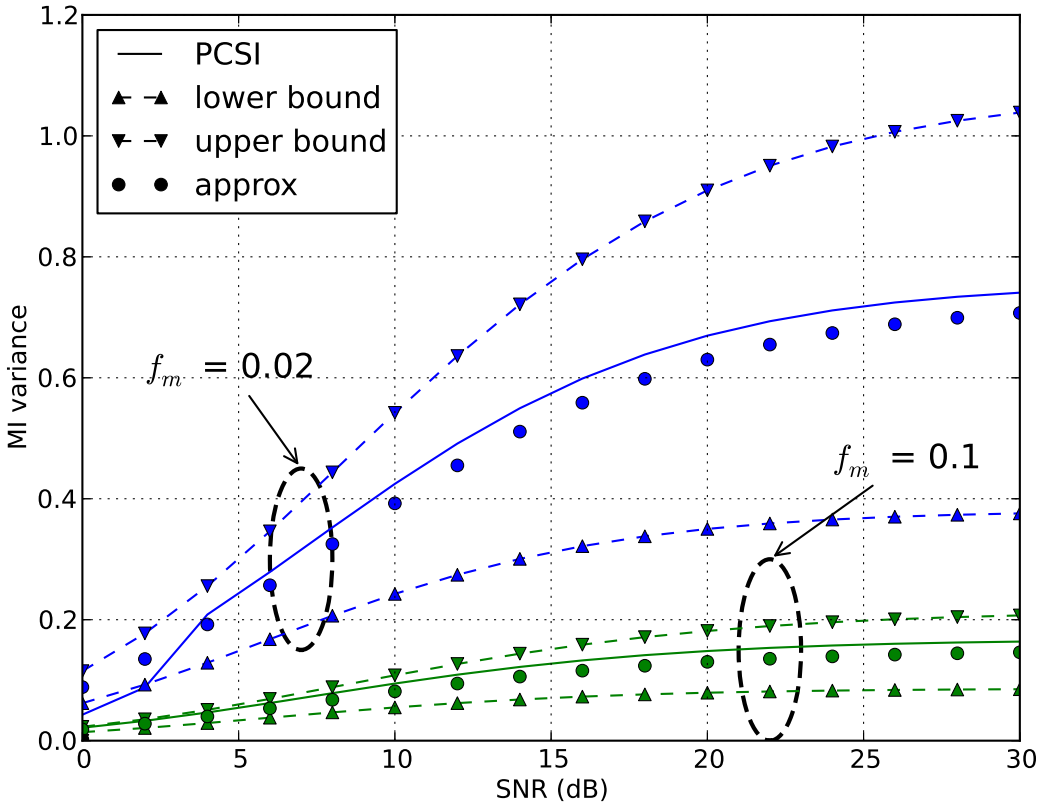

Figure 5.3: Mutual information variance versus SNR for two maximum normalized Dopplers. The "approx" curve is the average of the lower and upper bounds. The "knee" near SNR = 3 dB of the "PCSI" curve is due to limits in numerical precision.

5.4.1 PCSI

For the PCSI system, (5.13) bounds the variance and (5.14) is a simple approximation. Figure 5.3 shows the variance of the mutual information versus SNR for maximum normalized Dopplers of $f_m = 0.02$ and $f_m = 0.1$. It can be observed that the bounds become tighter for low SNR. The faster fading scenario with $f_m = 0.1$ shows less variance as the channel offers more diversity. The simple proposed approximation only slightly underestimates the true variance over the entire SNR interval.

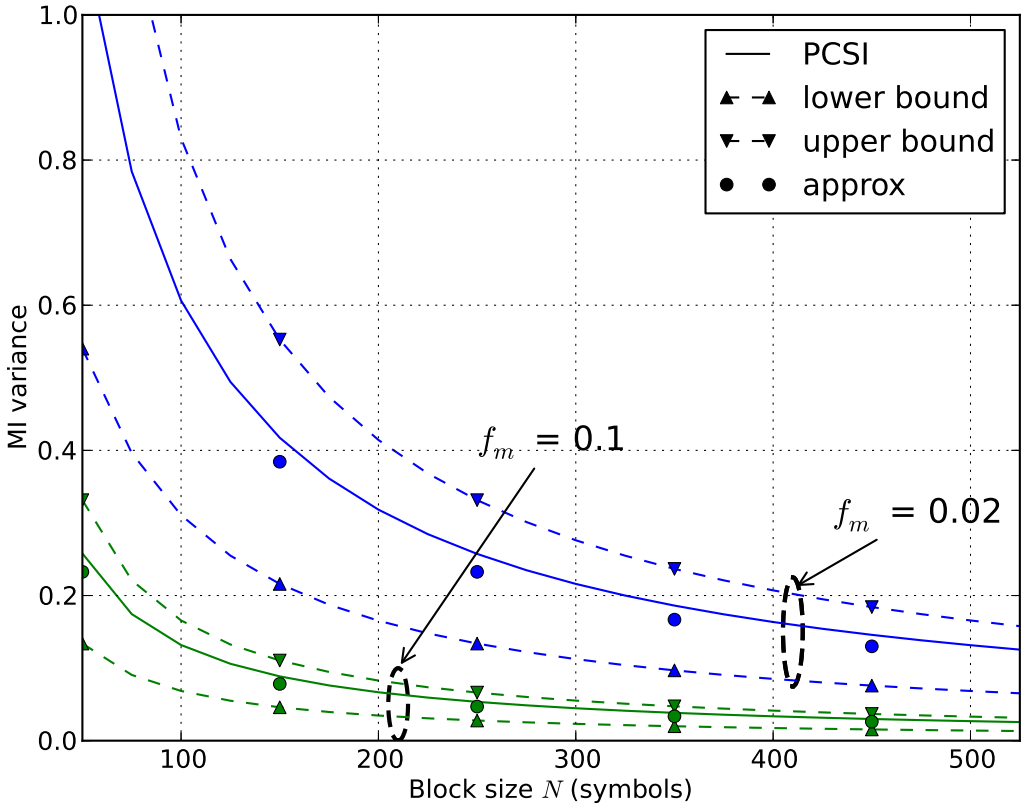

Figure 5.4: Outage probability versus block size N with PCSI for normalized maximum Dopplers $f_m = 0.02$ and $f_m = 0.1$.

Figure 5.4 shows the mutual information variance versus block size for a fixed SNR of 30 dB. This results in the loosest bounds in the SNR interval of interest. This figure mimics Figures 1 and 2 of [MSS08] which plot mutual information variance versus channel length for wideband OFDM over a channel with a uniform power-delay profile. The system model used in [MSS08] is the frequency-domain dual of that analyzed in this paper. However, here we are able to prove that the variance is inversely proportional to the block size (equivalently channel length in [MSS08]) rather than merely suggest it from the plot. Because the variance is a positive quantity and is bound from above by a function approaching 0 asymptotically with N, we conclude that the MI variance indeed approaches 0 asymptotically with the block size.

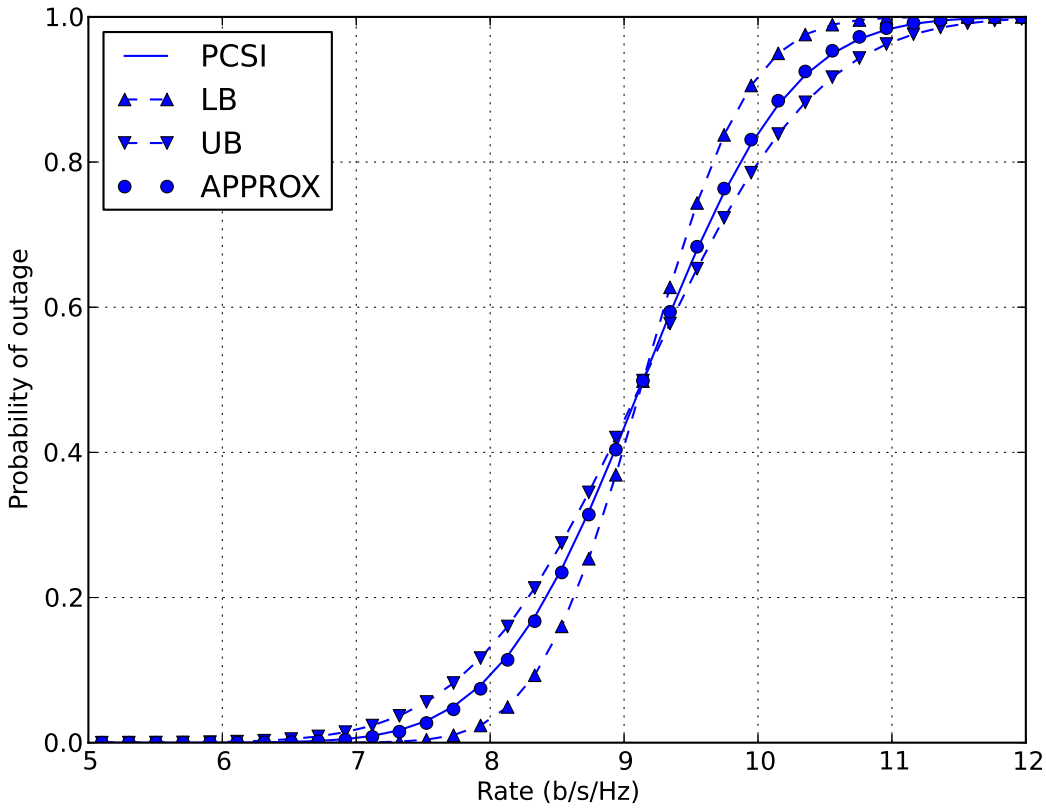

Figure 5.5: Outage probability versus rate with PCSI, SNR = 30 dB, and maximum normalized Doppler $f_m = 0.02$.

Figure 5.5 plots the outage cummulative distribution function (CDF) versus transmission rate for SNR = 30 dB and f_m = 0.02. Despite the looseness of the variance bounds at SNR = 30 dB, the CDFs resulting from the variance bounds are quite accurate. The CDF using the approximation overlaps the true CDF.

5.4.2 ECSI

For the ECSI analysis, the bounds (5.22) and corresponding approximation are not guaranteed to be valid due to the use of the PCSI weight function to approximate that for ECSI. The block size for these plots is $M = 5 \geq 1/2f_m \forall f_m \leq 0.1$. Though this sub-block size is quite small (see

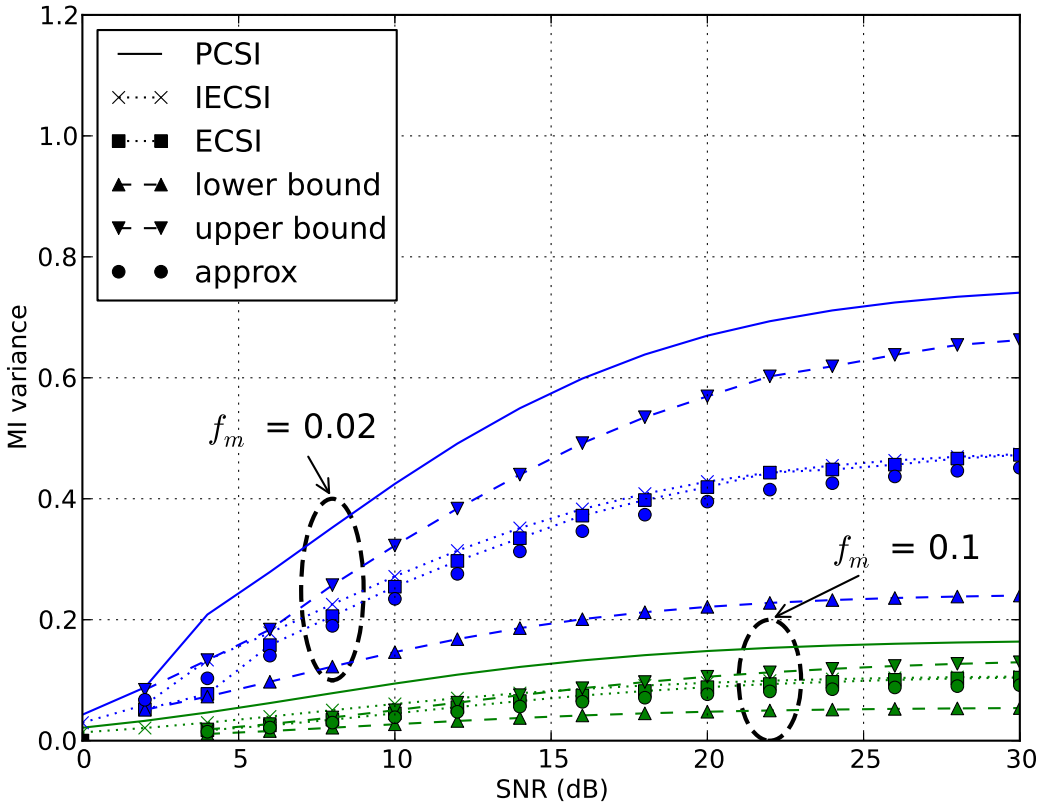

Figure 5.6: Mutual information variance versus SNR with ECSI for maximum normalized Doppler $f_m = 0.1$ and $f_m = 0.02$.

discussion of Figure 5.2), the results verify that the variance bounds (5.22) derived using the PCSI weights remain valid over a reasonable range of SNR and maximum normalized Doppler. The "PCSI" curves are included for comparison to those in Subsection 5.4.1.

Similar to the PCSI case, the CDFs in Figure 5.7 derived from the variance bounds and approximation closely track the true ECSI variance.

5.5 Conclusion

In this chapter we derived bounds and a simple approximation for the variance of the mutual information of a narrowband transmission over a time-varying channel in terms of the block

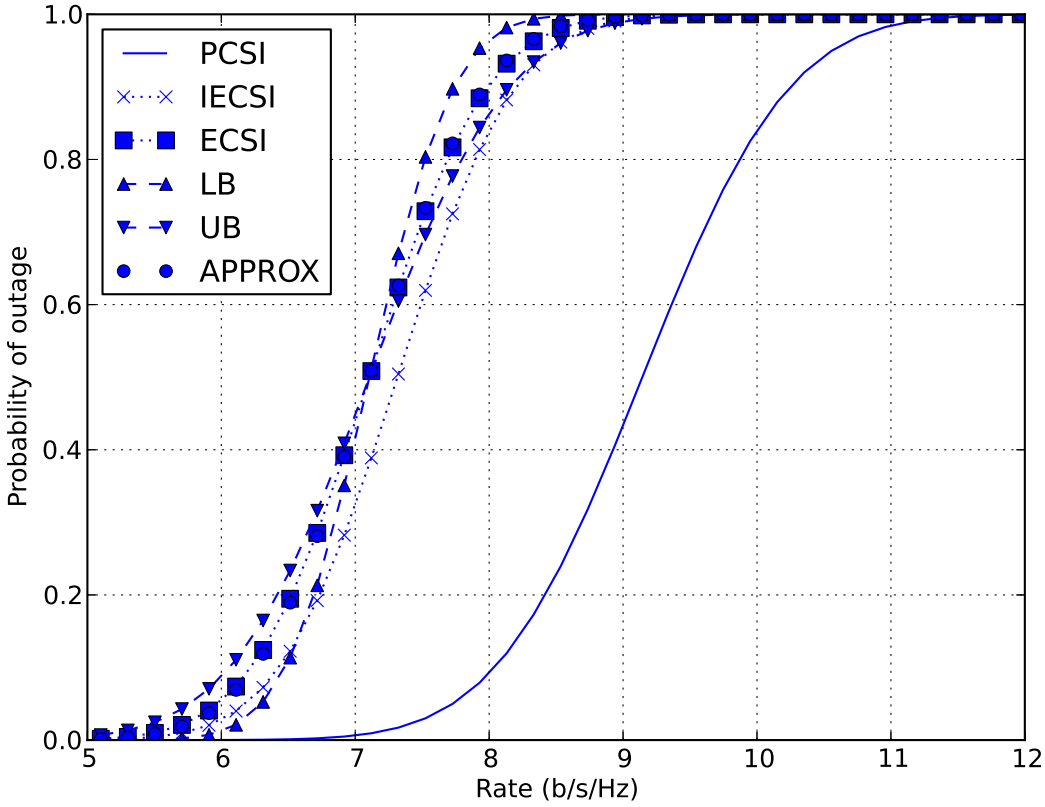

Figure 5.7: Outage probability versus rate with ECSI, SNR = 30 dB, and maximum normalized Doppler $f_m = 0.02$.

size and Doppler spectrum for receivers with PCSI and PSAM systems using ECSI. When the Doppler spectrum was flat, closed form bounds showed the intuitive inverse dependence of the variance on the number of sub-blocks in the transmission. This was shown to correspond to the behavior of a block-fading channel.

APPENDIX A

Derivation of (5.12) for Flat Doppler Spectrum

A.1 Derivation of (5.12) for Flat Doppler Spectrum

Substituting (5.3) for $S_H(e^{j\omega})$ in the convolution in (5.10)

$$(S_F * S_F)(e^{j\omega}) = \frac{\pi}{\omega_m}\,\mathrm{tri}\left(e^{j\omega/2\omega_m}\right) = \begin{cases} \frac{\pi}{\omega_m}\left(1-\frac{|\omega|}{2\omega_m}\right), & \omega \le 2\omega_m, \\ 0, & \text{otherwise}, \end{cases} \tag{A.1}$$

where $\omega_m = 2\pi f_m$ is the maximum Doppler shift in radians per second. The Fourier transform of the normalized triangle function is [MC91]

$$\mathcal{F}\left\{\frac{1}{c}\,\mathrm{tri}\left(\frac{x}{c}\right)\right\} = \mathrm{sinc}^2(c\omega/2). \tag{A.2}$$

Substituting the transform of the PCSI weight function (5.11) and (A.1) into (5.10)

$$\bar{a} = \frac{1}{2\omega_m}\int_{-2\omega_m}^{2\omega_m}\left(1-\frac{|\omega|}{2\omega_m}\right)\mathrm{sinc}^2\left(\frac{\omega N}{2}\right)\mathrm{d}\,\omega. \tag{A.3}$$

Using the result from Appendix B with $2\omega_m \Rightarrow b$, $N/2 \Rightarrow a$ we get

$$\bar{a} = \frac{2}{\omega_m N}\,\mathrm{Si}(2\omega_m N) - \mathrm{sinc}^2(\omega_m N) - \frac{\mathrm{Cin}(2\omega_m N)}{(\omega_m N)^2} \tag{A.4}$$

Using the following bounds for $2f_m N > N/M > K \ge 1$, which guarantees each block contains at least one pilot symbol, for each term in (A.4):

$$\frac{\pi}{2} + \frac{1}{x} \ge \mathrm{Si}(x) \ge \frac{\pi}{2} - \frac{1}{x} \tag{A.5}$$

$$\frac{1}{x^2} \ge \mathrm{sinc}^2(x) \ge 0 \tag{A.6}$$

$$\frac{x^2+1}{x} \ge \mathrm{Cin}(x) \ge \frac{x-2}{x} \tag{A.7}$$

and substituting $\theta = \omega_m N = 2\pi f_m N$ yields the result (5.12).

APPENDIX B

Integral solution for (A.3)

The integral of the form

$$\int_{-b}^{b}\left(1-\frac{|x|}{b}\right)\operatorname{sinc}^2(ax)\,\mathrm{d}x=\int_{-b}^{b}\operatorname{sinc}^2(ax)\,\mathrm{d}x-2\int_{0}^{b}\frac{x}{b}\operatorname{sinc}^2(ax)\,\mathrm{d}x \tag{B.1}$$

The first term can be solve via integration by parts with $u=\operatorname{sinc}^2(ax)$ and $\mathrm{d}v=\mathrm{d}x$

$$\begin{aligned}\int_{-b}^{b}\operatorname{sinc}^2(ax)\,\mathrm{d}x=2b\operatorname{sinc}^2(ab)-4\int_{-b}^{b}\frac{\sin(ax)\cos(ax)}{2ax}\,\mathrm{d}x\\ +2\int_{-b}^{b}\operatorname{sinc}^2(ax)\,\mathrm{d}x=\frac{2}{a}\operatorname{Si}(2ab)-2b\operatorname{sinc}^2(ab)\end{aligned} \tag{B.2}$$

where on the first line we moved the last term on the rhs to the lhs and recognized the second term on the rhs as $\operatorname{Si}(\cdot)$, the sine integral [AS72, 5.2.1].

The second integral in (B.1) is

$$\begin{aligned}\int_{0}^{b}\frac{x}{b}\frac{\sin^2(ax)}{(ax)^2}\,\mathrm{d}x&=\frac{1}{ab}\int_{0}^{b}\frac{1-\cos(2ax)}{2ax}\,\mathrm{d}x\\ &=\frac{1}{2a^2b}\int_{0}^{2ab}\frac{1-cos(y)}{y}\,\mathrm{d}y\end{aligned} \tag{B.3}$$

where in the last equality we substituted $y=2ax$. The integral in the last rhs is $\operatorname{Cin}(x)$, related to the cosine integral [AS72, 5.2.2].

REFERENCES

[AIT04] Guillermo Acosta, Mary Ann Ingram, and Kathleen Tokuda. "Measured Joint Doppler-Delay Power Profiles for Vehicle-to-Vehicle Communications at 2.4 GHz." In *Proc. IEEE GLOBECOM*, volume 6, pp. 3813–3817. IEEE, December 2004.

[APW09] Khaled Almustafa, Serguei Primak, Tricia Willink, and Kareem Baddour. "On Achievable Data Rates and Optimal Power Allocation in Fading Channels with Imperfect Channel State Information." *Wireless Personal Communications Journal*, **50**(1), 2009.

[AS72] Milton Abramowitz and Irene A. Stegun, editors. *Handbook of Mathematical Functions with Formulas, Graphs, and Mathematical Tables*. U.S. Government Printing Office, Washington, D.C. 20402, 10 edition, December 1972.

[Ass09] Antonio Assalini. "Maximizing outage capacity of OFDM transmit diversity systems." *IEEE Trans. Veh. Technol.*, **58**(9):4786–4794, November 2009.

[BT05] G. Bianchi and I. Tinnirello. "Remarks on IEEE 802.11 DCF performance analysis." *IEEE Commun. Lett.*, **9**(8):765–767, August 2005.

[CB04] Lingzhi Cao and N.C. Beaulieu. "Exact error-rate analysis of diversity 16-QAM with channel estimation error." *IEEE Trans. Commun.*, **52**(6):1019–1029, June 2004.

[Cla68] R H Clarke. "A statistical theory of mobile-radio reception." *Bell System Technical Journal*, **47**:975–1000, July 1968.

[CST07] Alan Clark, Peter J. Smith, and Desomond P. Taylor. "Instantaneous Capacity of OFDM on Rayleigh-Fading Channels." *IEEE Trans. Inf. Theory*, **53**(1):355–361, 2007.

[DF12] Jared Dulmage and Michael P. Fitz. "Channel Estimation, Overhead, and Outage for PSAM-OFDM." under review, August 2012.

[dlm12] "Digital Library of Mathematical Functions: Meijer G-Function." National Institute of Standards and Technology, March 2012. online, http://dlmf.nist.gov/16.17.E1.

[FGS99] M.P. Fitz, J. Grimm, and S. Siwamogsatham. "A new view of performance analysis techniques in correlated Rayleigh fading." In *Proc. IEEE WCNC*, pp. 139–144, September 1999.

[Grz89] JA Grzesik. "Von Neumann's Rejection Technique Reexamined." *SIAM Review*, **31**(3):486–489, September 1989.

[HH03] Babak Hassibi and Bertrand M. Hockwald. "How Much Training is Needed in Multiple-Antenna Wireless Links?" *IEEE Trans. Inf. Theory*, **49**(4):951–963, April 2003.

[HR03] Yuheng Huang and J.A. Ritcey. "16-QAM BICM-ID in fading channels with imperfect channel state information." *IEEE Trans. Commun.*, **2**(5):1000–1007, September 2003.

[IEE03] "Part 11: Wireless LAN Medim Access Control (MAC) and Physical Layer (PHY) specifications." ANSI/IEEE Std 802.11 1999 Edition (R2003), June 2003.

[IEE06] "Part 11: Wireless LAN Medim Access Control (MAC) and Physical Layer (PHY) specifications:Amendment 3: Wireless Access in Vehicular Environments (WAVE)." IEEE P802.11p/D1.0, February 2006.

[JC94] William C. Jakes and Donald C. Cox, editors. *Microwave Mobile Communications*. Wiley-IEEE Press, 1994.

[JL10] Nihar Jindal and Angel Lozano. "A Unified Treatment of Optimum Pilot Overhead in Multipath Fading Channels." *IEEE Trans. Commun.*, **58**(10):2939–2948, October 2010.

[Loz08] Angel Lozano. "Interplay of Spectral Efficiency, Power and Doppler Spectrum for Reference-Signal-Assisted Wirelees Communication." *IEEE Trans. Wireless Commun.*, **7**(12):5020–5029, December 2008.

[M00] Muriel Médard. "The Effect upon Channel Capacity in Wireless Communications of Perfect and Imperfect Knowledge of the Channel." *IEEE Trans. Inf. Theory*, **46**(3):933–946, May 2000.

[MC91] Clare D. McGillem and George R. Cooper. *Continuous and Discrete Signal and System Analysis*. Saunders College Publishing, 3 edition, 1991.

[MM01] Michele Morelli and Umberto Mengali. "A comparison of pilot-aided channel estimation methods for OFDM systems." *IEEE Trans. Signal Process.*, **49**(12), December 2001.

[MSS08] Matthew R. McKay, Peter J. Smith, Himal A. Suraweera, and Iain B. Collings. "On the Mututal Information Distribution of OFDM-Based Spatial Multiplexing: Exact Variance and Outage Approximation." *IEEE Trans. Inf. Theory*, **54**:3260–3278, July 2008.

[OG02a] Shuichi Ohno and Georgios B. Giannakis. "Average-Rate Optimal PSAM Transmissions Over Time-Selective Fading Channels." *IEEE Trans. Wireless Commun.*, **1**(4):712–720, October 2002.

[OG02b] Shuichi Ohno and Georgios B. Giannakis. "Optimal Training and redundant precoding for block transmissions with application to wireless OFDM." *IEEE Trans. Commun.*, **50**(12):2113–2123, December 2002.

[OG04] Shuichi Ohno and Georgios B. Giannakis. "Capacity Maximizing MMSE-Optimal Pilots for Wireless OFDM over Frequency-Selective Block Rayleigh-Fading Channels." *IEEE Trans. Inf. Theory*, **50**(9):2138–2145, September 2004.

[Pat06] Chirag S. Patel. *Wireless Channel Modeling, Simulation, and Estimation*. Ph.D. dissertation, Georgia Institute of Technology, March 2006.

[PKL98] Matthias Patzold, Ulrich Killat, Frank Laue, and Yingchun Li. "On the Statistical Properties of Deterministic simulation models for mobile fading channels." *IEEE Trans. Veh. Technol.*, **47**:254–269, February 1998.

[PL99] Matthias Patzold and Frank Laue. "Level-crossing rate and average duration of fades of deterministic simulation models for Rice fading channels." *IEEE Trans. Veh. Technol.*, **48**:1121–1129, 1999.

[Rap96] Theodore S. Rappaport. *Wireless Communications*. Prentice Hall PTR, 1996.

[SA95] M.G. Shayesteh and A. Aghamohammadi. "On the error probability of linearly modulated signals on frequency-flat Ricean, Rayleigh, and AWGN channels." *IEEE Trans. Commun.*, **43**(234):1454–1466, February 1995.

[SCE02] S. Sibecas, C.A. Corral, S. Emami, and G. Stratis. "On the suitability of 802.11a/RA for high-mobility DSRC." In *Proc. IEEE VTC*, volume 1, pp. 229–234, 2002.

[SCE03] S. Sibecas, C.A. Corral, S. Emami, G. Stratis, and G. Rasor. "Pseudo-pilot OFDM scheme for 802.11a and R/A in DSRC applications." In *Proc. IEEE VTC*, volume 2, pp. 1234–1237, October 2003.

[SCH07] Dan Stancil, Lin Cheng, Ben Henty, and Fan Bai. "Performance of 802.11p Waveforms over the Vehicle-to-Vehicle channel at 5.9 GHz." IEEE 802.11 Task Group report, September 2007.

[SL07] Krzysztof Szczypiorski and Józef Lubacz. *Managing Traffic Performance in Converged Networks*, volume 4516 of *Lecture Notes in Computer Science*, chapter Performance Evaluation of IEEE 802.11 DCF, pp. 1084–1095. Springer, September 2007.

[Stu01] Gordon L. Stuber. *Principles of Mobile Communication*. Kluwer Academic Publishers, Norwell, MA, USA, 2001.

[TAG99] Xiaoyi Tang, M.-S. Alouini, and A. Goldsmith. "Effect of channel estimation error on M-QAM BER performance in Rayleigh fading." In *Proc. IEEE VTC*, volume 2, pp. 1111–1115, July 1999.

[TC06] Giorgio Taricco and Giulio Coluccia. "Mismatched and optimum receivers for the correlated Rician fading MIMO channel." In *Proc. Allerton*, pp. 266–273, September 2006.

[WJ11] Peng Wu and Nihar Jindal. "Coding Versus ARQ in Fading Channels: How reliable should the PHY be?" *IEEE Trans. Commun.*, **59**(12):3363–3374, December 2011.

[YEY04] Jijun Yin, Tamer ElBatt, Gavin Yeung, Bo Ryu, Stephen Habermas, Hariharan Krishnan, and Timothy Talty. “Performance evaluation of safety applications over DSRC vehicular ad hoc networks.” In *Proc. IEEE VANET*, pp. 1–9, New York, NY, USA, 2004. ACM.